

Analyses of Planetary Atmospheres Across the Spectrum: From Titan to Exoplanets

Thesis by

Joshua A. Kammer

In Partial Fulfillment of the Requirements

for the Degree of

Doctor of Philosophy



California Institute of Technology

Pasadena, California

2015

(Defended September 25, 2014)

© 2014

Joshua A. Kammer

All Rights Reserved

For Science!

Acknowledgements

They say the journey of graduate school is a long and tortuous one - and yet, looking back, the path seemed inevitable. I have always harbored a love for the stars and everything related to space exploration, so I suppose it is only natural that I found myself here, working to help uncover a few more of the mysteries that the universe has thrown our way. I would not be here, however, without the inspiration and support of quite a few people, so I'd like to acknowledge just a few of them here.

First, I want to thank my parents, Mark and Madeline, for instilling in me a love for knowledge and an ineffable desire to explore the world in which we live. If I accomplish anything in life it is due to your love and support during my childhood. To be honest, I will depend on you even more once I have a family of my own, so don't think you're off the hook quite yet!

I also have to thank my fiancée, Whitney, for taking the plunge with me and starting a new life together in Colorado (and beyond). Home is where you are, and I am so thankful to have you at my side to face all the challenges of life together.

I was lucky to have arrived at Caltech at the same time as an amazing group of people. I'd like to thank my officemates for some great years of both working together and also going on adventures outside of Pasadena - of which road trips to Arizona, camping at Joshua Tree, and expeditions to Iceland are just a few. Mike Line, Alex Lockwood, Adam Waszczak, and Masha Kleshcheva, thanks for making life in and out of our office so fun and memorable. Also a special mention to my other fellow classmates, Peter Gao and Miki Nakajima - thanks for sharing in the journey. Graduate school doesn't last forever, but with friends like y'all, sometimes I wish it did!

I absolutely must thank both of my thesis advisors, Yuk Yung and Heather Knutson. Yuk, thank you - you've taught me a lot about academia, but even more about life in general. Sunday (and Monday, Wednesday, etc.) meetings were definitely character building exercises, but I wouldn't have had the same success without your guidance. Heather, thank you for introducing me to the wild world of exoplanets. There aren't many things more exciting than discovering and characterizing the thousands upon thousands of new worlds out there in the galaxy, and I hope to be a part of that again some day soon.

Lastly, I'd like to thank the other members of my thesis committee: Andy Ingersoll and Geoff Blake. Thanks for your additional teaching and guidance over the years here at Caltech.

Abstract

Planetary atmospheres exist in a seemingly endless variety of physical and chemical environments. There are an equally diverse number of methods by which we can study and characterize atmospheric composition. In order to better understand the fundamental chemistry and physical processes underlying all planetary atmospheres, my research of the past four years has focused on two distinct topics. First, I focused on the data analysis and spectral retrieval of observations obtained by the Ultraviolet Imaging Spectrograph (UVIS) instrument onboard the *Cassini* spacecraft while in orbit around Saturn. These observations consisted of stellar occultation measurements of Titan's upper atmosphere, probing the chemical composition in the region 300 to 1500 km above Titan's surface. I examined the relative abundances of Titan's two most prevalent chemical species, nitrogen and methane. I also focused on the aerosols that are formed through chemistry involving these two major species, and determined the vertical profiles of aerosol particles as a function of time and latitude. Moving beyond our own solar system, my second topic of investigation involved analysis of infra-red light curves from the *Spitzer* space telescope, obtained as it measured the light from stars hosting planets of their own. I focused on both transit and eclipse modeling during *Spitzer* data reduction and analysis. In my initial work, I utilized the data to search for transits of planets a few Earth masses in size. In more recent research, I analyzed secondary eclipses of three exoplanets and constrained the range of possible temperatures and compositions of their atmospheres.

Contents

Acknowledgements	iv
Abstract	v
List of Figures	viii
List of Tables	x
1 Preface	1
1.1 Introduction	1
1.2 <i>Cassini</i> and Titan	1
1.3 Exoplanet Surveys and Atmospheric Characterization	2
2 Observations and Modeling of Hydrocarbons in Titan’s Upper Atmosphere	6
2.1 Summary	6
2.2 Introduction	6
2.3 The UVIS Instrument	7
2.4 Retrieval Methodology and Results	7
2.5 Photochemical Modeling	11
2.6 Conclusions	15
2.7 Acknowledgements	15
3 Composition of Titan’s Upper Atmosphere from Cassini UVIS EUV Stellar Oc-	
 cultations	19
3.1 Summary	19
3.2 Introduction	19
3.3 The UVIS Instrument	21
3.3.1 FUV and EUV Spectrographs	21
3.3.2 Instrument Model	21
3.3.3 Spacecraft Pointing Issues	21

3.3.4	Occultation Spatial/Seasonal Coverage	22
3.4	Methodology	22
3.4.1	Forward Model	22
3.4.2	Retrieval Algorithm	23
3.4.3	Conversion from Abundance to Density Profiles	26
3.4.4	Effective Temperatures from Fits to N ₂ Scale Height	26
3.5	Results and Discussion	29
3.5.1	Retrieved Abundance and Density Profiles	29
3.5.2	Effective Temperatures	29
3.6	Conclusions	32
3.7	Acknowledgements	32
4	Atmospheric Profiles of Titan’s High-Altitude Haze: <i>Cassini</i> UVIS Stellar Oc-	
	cultation Measurements	36
4.1	Summary	36
4.2	Introduction	36
4.3	<i>Cassini</i> UVIS Stellar Occultation Observations	37
4.3.1	Titan Flybys	37
4.3.2	Wavelength Selection	38
4.4	UVIS Data Acquisition and Reduction Methodology	38
4.5	Discussion	39
4.6	Conclusions	44
4.7	Acknowledgements	44
5	A <i>Spitzer</i> Search for Transits of Radial Velocity Detected Super-Earths	47
5.1	Summary	47
5.2	Introduction	48
5.3	Target System Properties and Radial Velocity Measurements	49
5.3.1	System Properties	49
5.3.2	Radial Velocity Ephemerides	50
5.4	<i>Spitzer</i> Data Acquisition and Reduction Methodology	52
5.4.1	Photometry and Intrapixel Sensitivity	52
5.4.2	Transit Models and Uncertainty Estimation	53
5.5	Discussion	57
5.6	Conclusions	57
5.7	Acknowledgements	59

6	<i>Spitzer</i> Secondary Eclipse Observations of Three New Cool Gas Giant Planets	62
6.1	Summary	62
6.2	Introduction	63
6.3	Observations and Data Analysis	65
	6.3.1 Photometry and Intrapixel Sensitivity	65
	6.3.2 Eclipse Models and Uncertainty Estimation	68
6.4	Discussion	68
6.5	Conclusions	69
6.6	Acknowledgements	70

List of Figures

1.1	Observed Change in Photon Flux with Ray Height	3
1.2	<i>Spitzer</i> Surveyed Super-Earths	5
2.1	Optical Depth as Function of h and λ	9
2.2	Model Fits at Different Heights	10
2.3	Density Profiles of Hydrocarbon Species	12
2.4	Comparison with Voyager 1 Data	13
2.5	Comparison of Model Fits to Observations	14
3.1	Raw UVIS Spectra for T41-I	24
3.2	Contour Map of Grid Search Method	25
3.3	Marginalized Posteriors for Nitrogen and Methane	27
3.4	Nitrogen and Methane Line of Sight Abundances	27
3.5	Nitrogen and Methane Density Profiles	28
3.6	Ensemble of Results	30
3.7	Comparison with INMS Data	31
4.1	Analysis of T21, T23, and T35	40
4.2	Analysis of T40, T41-I, and T41-II	41
4.3	Analysis of T47-I, T47-II, and T48	42
4.4	Analysis of T52, T53, T56, and T58	43
5.1	Raw <i>Spitzer</i> Light Curves	54
5.2	Normalized <i>Spitzer</i> Light Curves	55
5.3	Histograms of Best Fit Planetary Radii	56
5.4	Detection Threshold as Function of Impact Parameter	58
6.1	Raw <i>Spitzer</i> 3.6 and 4.5 μm Data	66
6.2	Normalized <i>Spitzer</i> 3.6 and 4.5 μm Data	67
6.3	Effect of Atmospheric Metallicity	71

6.4	Models with Higher Metallicity	72
6.5	Models with Atmospheric Inversion	73

List of Tables

3.1	Analyzed Stellar Occultations	22
4.1	Titan Stellar Occultations	38
5.1	Target System Properties	50
5.2	<i>Spitzer</i> Observation Details	51
5.3	Limits on Transit Probability	51
6.1	Target System Properties	64
6.2	<i>Spitzer</i> Observation Details	64
6.3	Best Fit Eclipse Model Results	65

Chapter 1

Preface

1.1 Introduction

An atmosphere (or lack thereof) is perhaps a planet's most defining feature. It exists as the boundary between the bulk mass of a planet and the vacuum of space, often existing at a range of temperatures and pressures that provide myriad pathways for planets' chemical and physical evolution. Our solar system hosts a wide variety of atmospheres, from nearly airless bodies like Mercury or the Moon, to massive gas giants like Jupiter. Here on Earth, our atmosphere is fundamental to sustaining life as we know it, from the oxygen we breathe to the ozone layer that helps block harmful radiation from reaching the surface, so it is no surprise that we spend so much time and effort studying Earth's atmosphere in great detail. On the other hand, the study of other planets' atmospheres allows us to put that of Earth in better context, as well as to improve the physical equations on which we base our theoretical models of atmospheric behavior, wherever they exist in the universe.

This thesis focuses on atmospheric observational studies for two categories of planetary bodies. Chapters 2, 3, and 4 involve analyses of the upper atmosphere of Titan, Saturn's largest moon. The analyzed data is acquired during UV stellar occultation observations by the *Cassini* spacecraft, currently in orbit around Saturn. Moving beyond our own solar system, Chapters 5 and 6 examine recent studies in the relatively new field of exoplanets and exo-atmospheres. §1.2 and §1.3 describe more of the background of these projects in greater detail. Each chapter stands on its own as either an accepted journal article (with citation) or an article in preparation.

1.2 *Cassini* and Titan

Since the arrival of the *Cassini* spacecraft in 2004, we have acquired a wealth of new information about the Saturnian system. This is particularly true for Titan, as over 100 flybys of the moon have occurred in the past decade. There are many instruments onboard *Cassini*, each with its own unique investigative strengths, but the instrument suite used in this work is the Ultraviolet Imaging

Spectrograph (UVIS). The basic capabilities of this instrument allow for analysis of both emission and absorption features in the extreme and far ultraviolet wavelengths (EUV and FUV, combined coverage from 500 - 2000Å). For probing the composition of Titan’s upper atmosphere, the spacecraft was oriented during flybys such that the UVIS instrument detects the light from a UV-bright star, and then measures the intensity of this source as Titan passes in front of it. This basic geometry can be visualized in Figure 1.1. By measuring how ultraviolet light is absorbed at various wavelengths, information about the composition of Titan’s atmosphere can then be inferred based on the known cross-sections of absorption for various chemical species.

The starlight observed by UVIS passes through several layers in Titan’s atmosphere, and so is sensitive to multiple levels simultaneously. To deconvolve this effect and determine the local density of a given chemical species with altitude, I utilized the well-known equation that relates the line of sight abundance of a molecule as a function of ray height to the local number density as a function of altitude, given a spherically symmetric atmosphere. This relationship is shown in Equation 1.1, where $\rho(r)$ is the density at altitude r as measured from Titan’s center, and $\eta(y)$ is the measured line of sight abundance at ray height y .

$$\rho(r) = -\frac{1}{\pi} \int_r^\infty \frac{d\eta(y)}{dy} \frac{dy}{\sqrt{y^2 - r^2}} \quad (1.1)$$

Chapters 2, 3, and 4 go into further detail on my research utilizing this technique.

1.3 Exoplanet Surveys and Atmospheric Characterization

The study of planets beyond our solar system has advanced rapidly in the last decade. Both ground- and space-based observatories have discovered thousands of planets that exist in a wide variety of stellar environments. The planets themselves range from small, rocky terrestrial planets up to massive gas giants, and they are found at practically all distances from their host stars. The two primary techniques used to discover and characterize exoplanets are radial velocity measurements and transit surveys. The radial velocity method takes advantage of the gravitational interaction between a host star and its planet. While we often think of a planet orbiting a star, in reality the two bodies orbit their common center of mass. For that reason, relative to an outside observer the star may have an oscillating motion resulting in red or blue shifting of its spectral lines. By measuring the width of this shift, we can infer the presence of a planet and know something about the planet/star mass ratio. The relevant equation in this case is for the radial velocity semi-amplitude of the star, given by Equation 1.2, where G is the gravitational constant, P is the period of the planet’s orbit, m_p is the planet mass, m_* is the stellar mass, i is the orbital inclination with respect to the observer, and e is the orbital eccentricity.

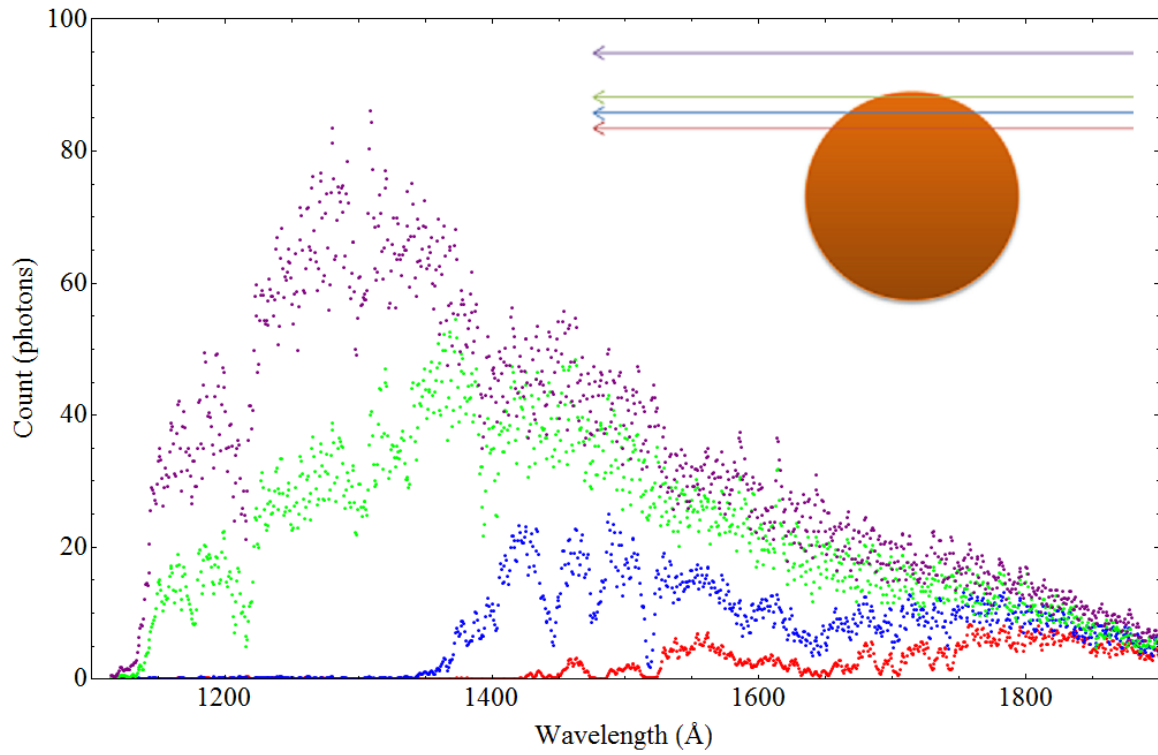


Figure 1.1 : The observed spectra of a UV-bright star as seen by UVIS at several different ray heights. The spectrum acquired above Titan's atmosphere (purple) corresponds to unfiltered starlight, while three spectra acquired at levels deeper in Titan's atmosphere (green, blue, red) show increasing amounts of absorption.

$$K = \left(\frac{2\pi G}{P} \right)^{1/3} \frac{m_p \sin i}{m_*^{2/3}} \frac{1}{\sqrt{1-e^2}} \quad (1.2)$$

The second method works for planets that are found to transit, or pass in front of, their host stars. In these instances, some amount of starlight is blocked by the planet, and we can infer information about the planet both from the depth of the transit as well as its duration and shape. In addition, a similar dip in detected light occurs when a planet passes behind the star around half an orbit later; this is called a secondary eclipse. The wavelength dependency of transit or eclipse depth is used to determine the properties of the planet's atmosphere, based on models for how the atmosphere emits or absorbs light.

Chapter 5 describes my work on searching for transits of super-Earth sized planets utilizing data from the *Spitzer* space telescope. The planets shown in Figure 1.2 had already been discovered in radial velocity surveys, but if found to transit, would have possibly provided a rare chance to study the atmospheres of planets in this size range, as only a handful have been characterized thus far. Though no transits were detected, this approach is still valuable in finding planets like Earth that have characterizable atmospheres, and may yield more results in the future.

Spitzer can also be used to observe secondary eclipses, and in Chapter 6, I analyze eclipse light curves for three gas giant planets with relatively cooler temperatures ($\sim 1000\text{K}$), estimating the relative emission in the 3.6 and 4.5 μm bands in order to test the predictions of equilibrium chemistry models. These three targets are just a handful from a larger sample that will provide better insight into trends among exoplanets in this size and temperature range.

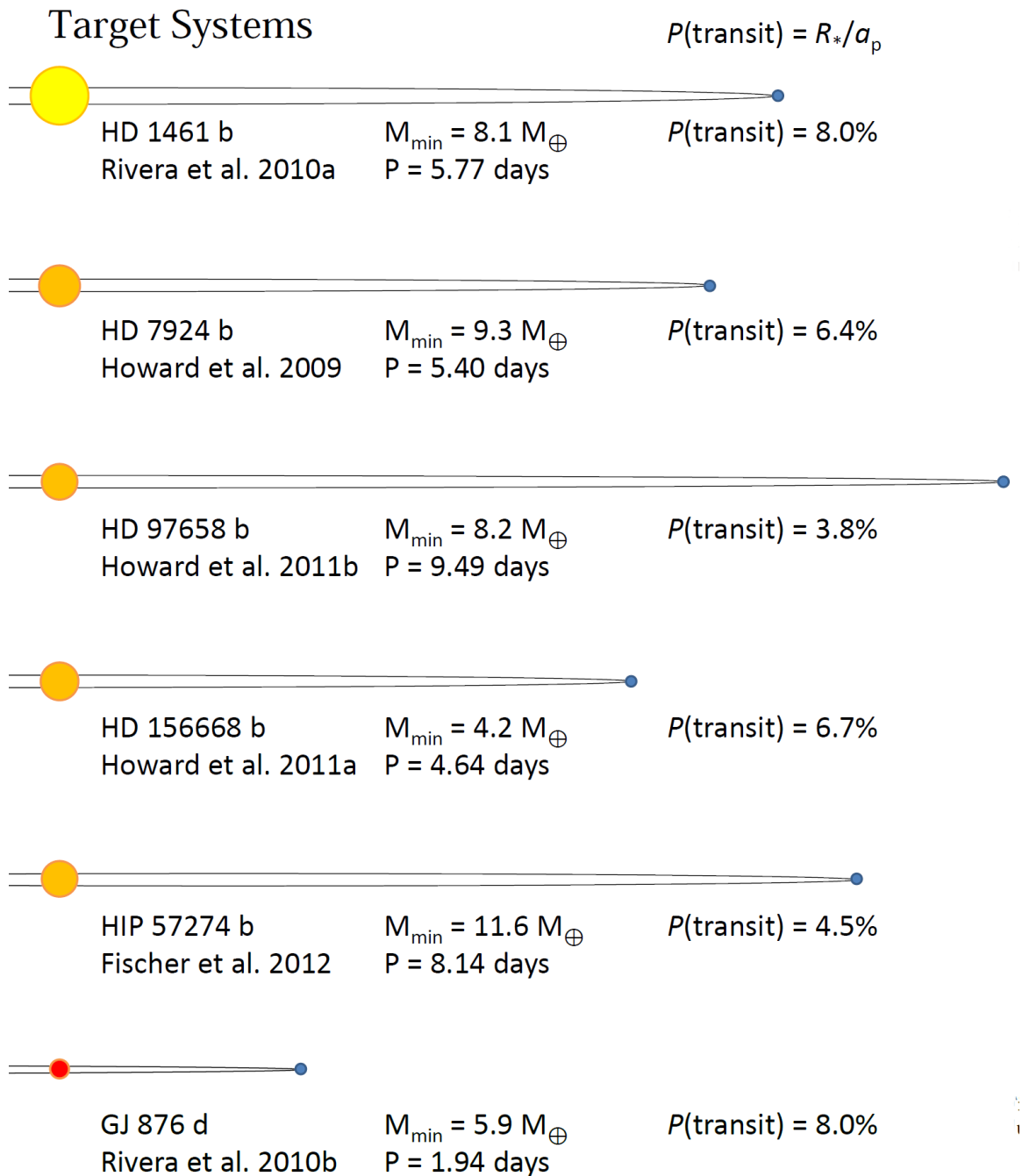


Figure 1.2 : These six targets were detected through radial velocity measurements, and had some *a priori* probability of also transiting (shown at right, estimated as the ratio of stellar radius to planet semi-major axis). Stellar radius and planet semi-major axis are shown to scale. Additional information in Chapter 5.

Chapter 2

Observations and Modeling of Hydrocarbons in Titan's Upper Atmosphere

2.1 Summary

We extract hydrocarbon and nitrile vertical profiles in the range 300 - 1200 km from *Cassini*-UVIS stellar occultation measurements at Titan and utilize them to constrain global chemical model calculations. The species analyzed are CH₄, C₂H₂, C₂H₄, C₄H₂, C₆H₆, HCN, HC₃N, and the end-product tholins. The derived profiles are found to be in good agreement to those of the *Cassini* INMS and CIRS experiments, which probe the regions above 1000 km and below 400 km, respectively. The results of a chemical model parameterized to fit the UVIS observations show the total mass production rate of tholins to be $1.5 \cdot 10^{-13} \text{ g cm}^{-2} \text{ s}^{-1}$, larger than previous estimates. Significant structure is apparent in the hydrocarbon and tholin density profiles and can be only roughly approximated by current modeling.

2.2 Introduction

Titan is one of the largest and most distinctive moons in our Solar System, and its atmosphere in particular has been the object of significant study in the Cassini mission to Saturn. Measurements of the state of the atmosphere include those of Flasar et al. (2005) and Waite et al. (2005). *Cassini* UVIS occultation results have been reported earlier by Shemansky et al. (2005), as well as Liang et al. (2007). Research on atmospheric evolution and structure has been reviewed extensively by Brown et al. (2009). The atmosphere has evolved into its current state through complex photochemical processes (Strobel, 1982; Yung et al., 1984; Wilson and Atreya, 2003), involving nitrogen (N₂) and methane (CH₄), the dominant molecular species in the atmosphere. It has been proposed that

this mixture may be analogous to what existed on the early Earth, as it certainly provides a rich abundance of hydrocarbons from which early life may have arisen (Coustenis and Taylor, 1999; Lunine, 2005).

Modeling the physical chemistry of Titan’s atmosphere is an area of active research (Lavvas et al., 2008a; Krasnopolsky, 2009). Tholins and other aerosols are a primary end product of Titan’s atmospheric chemistry (Khare et al., 1984), and much effort has gone into modeling its formation in order to better understand the chemistry involved (Wilson and Atreya, 2003; Liang et al., 2007). Models improve as observations better constrain both the composition and spatial and temporal variability of Titan’s atmosphere. Among the Cassini experiments, the Ultraviolet Imaging Spectrograph (UVIS) provides one of the few direct probes of the region between 300 km and 1000 km in altitude where much of the photochemistry on Titan occurs.

2.3 The UVIS Instrument

Cassini-UVIS has provided an abundance of data on the Saturn system since orbital insertion (Esposito et al., 2005). Several of these observations include solar and stellar occultation events through the upper atmosphere of Titan. The wealth of this information from UVIS has proven a challenge to analyze as quickly as it has been acquired; as a result there are a large number of occultation data sets that have been only partially reduced.

A full description of the UVIS experiment is contained in Esposito et al. (2004). The spectral range of the UVIS instrument is 563 - 1182Å(EUV) and 1115 - 1912Å(FUV). It is in the FUV range that the stellar occultation data sets are examined here, as this region provides strong absorption features of the hydrocarbon species detected in Titan’s atmosphere. The species analyzed in the absorption spectra that follow are CH₄ (methane), C₂H₂ (acetylene), C₂H₄ (ethylene), C₄H₂ (diacetylene), C₆H₆ (benzene), HCN (hydrogen cyanide), HC₃N (cyanoacetylene), and tholins.

Over 20 stellar and solar occultation events were observed from 2004 through 2009, and are referenced by the Titan flyby label (e.g., Tb or T10). The Tb and T21 stellar occultations, as well as solar occultations T10, T26, and T32, have been previously analyzed (Shemansky et al., 2005). The stellar occultations analyzed in this work include two from the Tb flyby in 2004 and one from the T21 flyby in 2006, as well as two from the T41 flyby in 2008. Others continue to be processed, and will be explored in greater depth in future work.

2.4 Retrieval Methodology and Results

The process of retrieving hydrocarbon densities from the raw observational data is carried out in three steps. Records from the UVIS instrument initially consist of integrated stellar flux for each

wavelength bin in the FUV region, generally acquired over a 2 km to 20 km step in occultation ray height, depending on the relative motion of the Cassini spacecraft, Titan, and the pointing direction of the star. An absorption spectrum is then calculated using Equation 2.1, where $\tau(\lambda, h)$ is the line of sight optical depth for a given ray height h and wavelength λ , $I(\lambda, h)$ is the stellar flux at that height and wavelength, and $I_0(\lambda)$ is the UV spectrum of the star measured above the atmosphere.

$$\tau(\lambda, h) = -\ln\left(\frac{I(\lambda, h)}{I_0(\lambda)}\right) \quad (2.1)$$

A profile of optical depth as a function of wavelength and occultation ray height is shown in Figure 2.1. Significant structure is immediately apparent, but the observed spectra are the effective result of cumulative absorption by a mix of species in the spectrograph line of sight. The partitioning of the species contributing to the observed spectrum depends on a forward modeling process that produces a best fit of cross-section vectors of the species recognized to be present in the observed spectrum. These cross-sections are obtained from laboratory work at several facilities, including temperature dependence where available (Shemansky et al., 2005; Vervack et al., 2004).

After processing with an instrument simulation code, a forward model for conversion of species abundances to optical depth is constructed. The model vectors are then adapted for use in a fitting algorithm derived from the work of Rodgers (2000). This algorithm utilizes an *a priori* estimate of the species abundances and iterative minimization of a cost function shown in Equation 2.2.

$$J(x) = (x - x_a)^T S_a^{-1} (x - x_a) + (y - Kx)^T S_e^{-1} (y - Kx) \quad (2.2)$$

In this case, y is the observed absorption spectrum and Kx is a linearization of the forward model of this spectrum; x is the vector describing the hydrocarbon abundances at a given height, and x_a is the *a priori* estimate of these abundances. S_a and S_e are the covariance matrices for the *a priori* estimate and the observational data, respectively, and represent the uncertainty in each. Lastly, K is the Jacobian matrix for each species, describing the relative change in optical depth observed at a given wavelength with a corresponding change in abundance.

Several examples of results of this fit at different heights in the Titan atmosphere are shown in Figure 2.2. At levels above 1000 km, background noise is a limiting factor, and generally only CH_4 can be retrieved satisfactorily. Optical depths larger than 5 are generally at the dynamic range limit in signal measurement. This constrains measurements of CH_4 to above 700 km, while other species are accessible down to 400 km or below, depending on absorption vector properties.

The final step in reduction is extraction of vertical density profiles from the abundance profiles using an inverse Abel transform method, assuming a spherically symmetric atmosphere. The profiles are shown in Figure 2.3 for the hydrocarbons CH_4 , C_2H_2 , C_2H_4 , C_4H_2 , C_6H_6 , HCN, HC_3N , and tholin, with comparison to the INMS (Magee et al., 2009) and CIRS (Vinatier et al., 2010) instrument

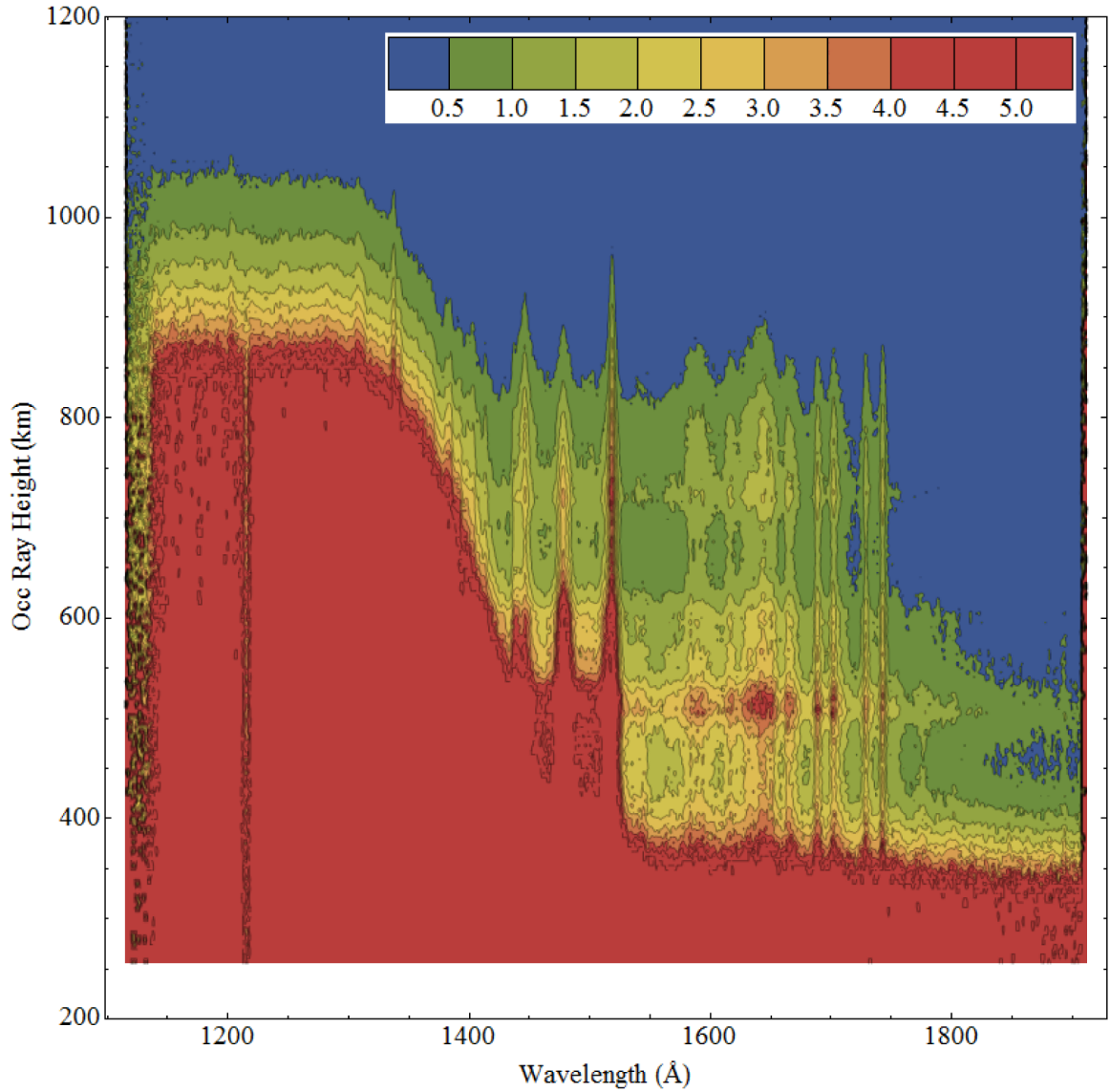


Figure 2.1 : Stellar occultation of star ϵ CMA during Titan ingress flyby T41. This contour plot shows line of sight optical depth from $\tau \leq 0.5$ (blue) to $\tau \geq 5.0$ (red) in interval steps of 0.5. Distinct horizontal layers of relatively higher optical depth are apparent at around 725 km and 500 km. Major features include the broad absorption region below 1400Å dominated by CH_4 , while the distinct peaks between 1400Å and 1800Å primarily correspond to a combination of C_2H_2 , C_2H_4 , and C_4H_2 . Below about 400 km the rest of the FUV region is absorbed by tholins.

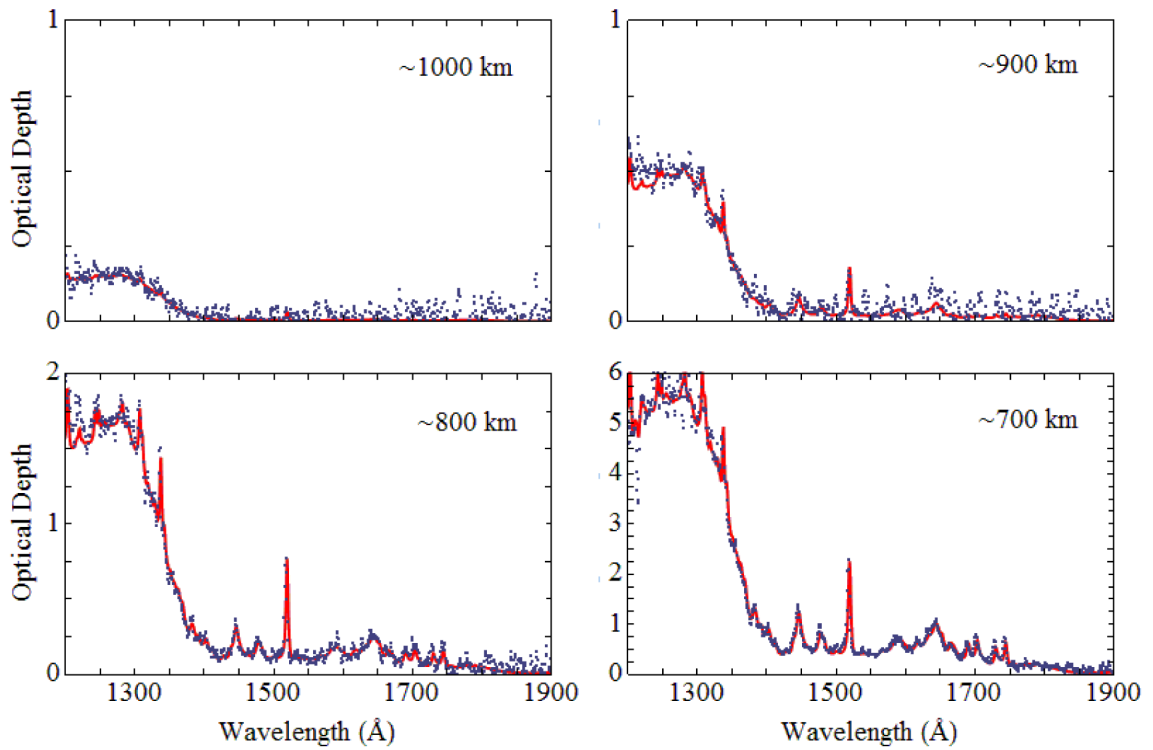


Figure 2.2 : Model fit (red) to UVIS optical depth data (blue) from the T41 ingress stellar occultation. Each plot corresponds to a different occultation ray height in Titan's atmosphere - 1000 km, 900 km, 800 km, and 700 km, respectively.

measurements.

The tholin vertical profiles shown in Figure 2.3 show layered structure in the 700 - 800 km and 400 - 500 km regions. The inversion structure in the 700 - 800 km region was first recognized by Smith et al. (1982) in a Voyager 1 solar occultation in 1980, indicating that this is a persistent feature. A comparison of the UVIS and Voyager 1 lightcurves is shown in Figure 2.4. The implication of an inversion is a severe reduction in the extinction at the pause in the occultation profile. In these regions the tholins are inferred to be depleted by orders of magnitude relative to the regions immediately above and below, suggesting strong regional loss processes and vertically distributed production of the species. The solar He II 304Å line has an optical depth of 25 at 750 km, so this feature could not be responsible for tholin destruction. The physical implication of this severe depletion is that tholin particles are entirely regenerated immediately below, possibly with composition and size differences from the particles above. A uniform particle extinction cross section was assumed in the derivation of the tholin vertical density profile. Some hydrocarbon species above the order of CH₄ tend to show population peaks in the vicinity of 750 km and depleted populations at lower altitudes with no evident inverted extinction curves.

2.5 Photochemical Modeling

A one dimensional Caltech/JPL photochemistry-transport model (Yung et al., 1984; Yung, 1987; Moses et al., 2000; Liang et al., 2007) is applied to simulate the diurnally-averaged vertical distributions of major gas species and tholin from 50 to 1500 km. 83 species are selected, along with 88 photo-dissociation and about 410 neutral chemical reactions. Eddy diffusivity is the same as in Liang et al. (2007). In order to explain the observed CH₄ abundances in the upper atmosphere, the volume mixing ratio of methane at the lower boundary is fixed as 2.5%, which is larger than the CIRS observed value of 1.6% (Flasar et al., 2005). Consistent with previous studies (Yelle et al., 2006, 2008; Liang et al., 2007), the scale height of the simulated CH₄ density profile is generally larger than the observations above 1000 km (Figure 2.5, CH₄, dashed line). One way to resolve this is to apply a maximum (diffusion-limited) methane escape flux ($\sim 5.5 \cdot 10^9$ cm s⁻¹ in this case) at the upper boundary, as suggested by Yelle et al. (2008). Alternatively, ionosphere physical chemistry can also be introduced to increase loss rates. Making use of diffusion-limited upward flux for all species allows the scale height of the methane density profile to be more consistent with the observations (Figure 2.5, CH₄, solid line).

The primary purpose of this model is to explain empirically the abundances of tholin and hydrocarbons simultaneously. The tholin radius in our model is assumed to be a constant value of ~ 7.6 nm, which is the monomer size derived from solar scattering observations. A Stokes settling velocity on the order of 0.1 cm s⁻¹ (Cabane et al., 1992; Lavvas et al., 2010) is used for tholin dry

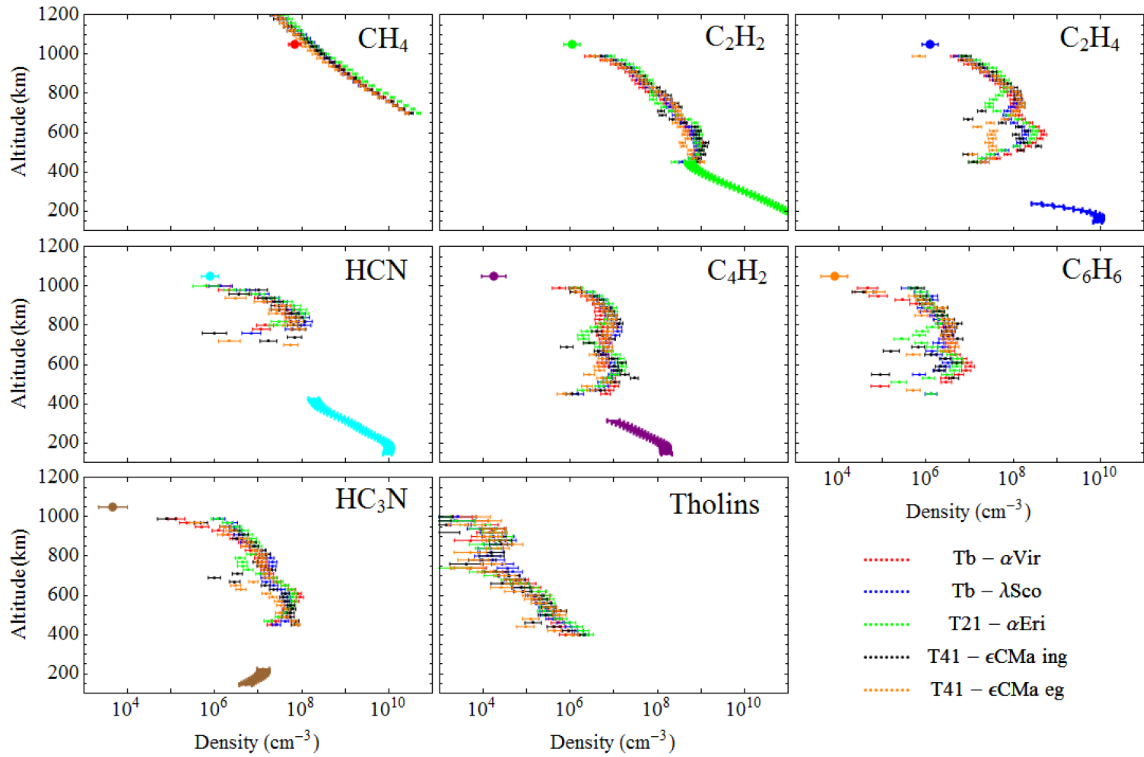


Figure 2.3 : Plots of hydrocarbon density retrievals for 5 stellar occultations: Tb - α Vir (red), Tb - λ Sco (blue), T21 - α Eri (green), T41 - ϵ CMa ingress (black) and T41 - ϵ CMa egress (orange). Also shown are INMS globally averaged densities at 1050 km (Magee et al., 2009), as well as CIRS data below 400 km for C₂H₂, C₂H₄, HCN, C₄H₂, and HC₃N at a latitude of 20.5 South during T27 (Vinatier et al., 2010). The UVIS retrieval results appear to be roughly consistent with those of both INMS and CIRS.

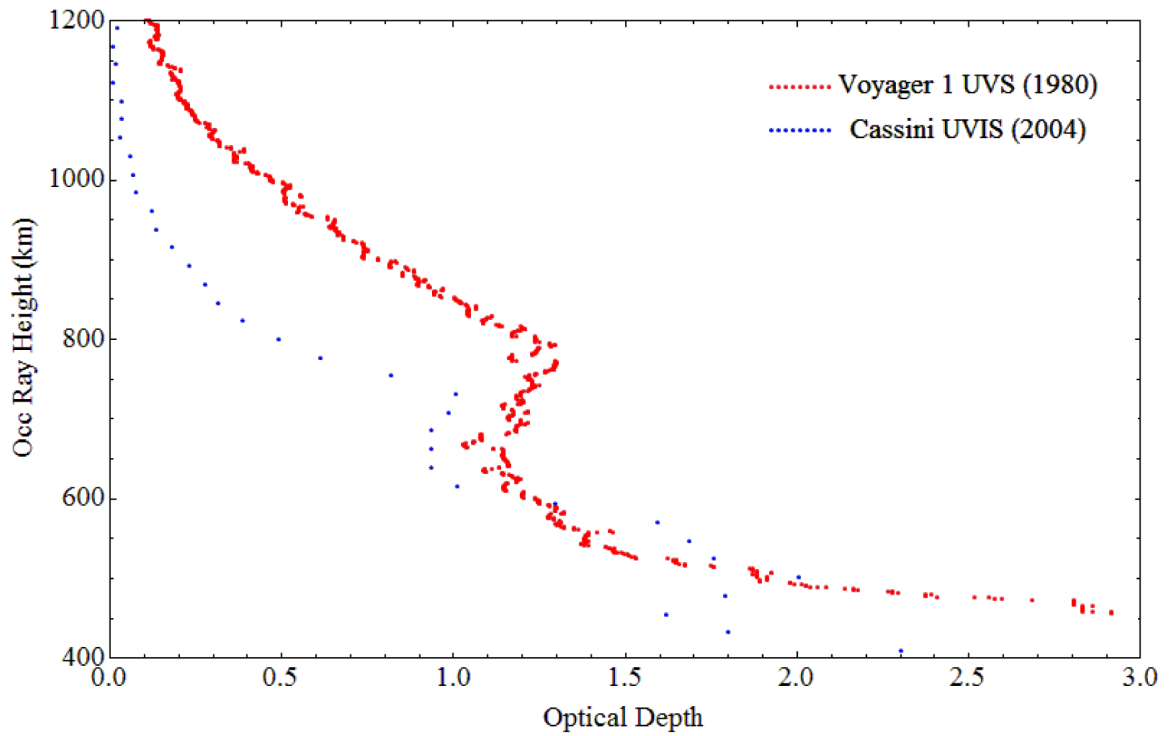


Figure 2.4 : The panel shows comparison of the extinction light curves from the Voyager 1 solar occultation 1980 DOY 318, latitude 2.74 North, and Cassini UVIS stellar occultation at Tb 2004 DOY 348, latitude 35.9 South. The photometric curves were centered at $\sim 1650 \text{ \AA}$. The curves show some differences in extinction level but both have a common inversion structure between the altitudes 700 and 800 km, indicating that the tholin vertical structure in this region is a temporally stable structure.

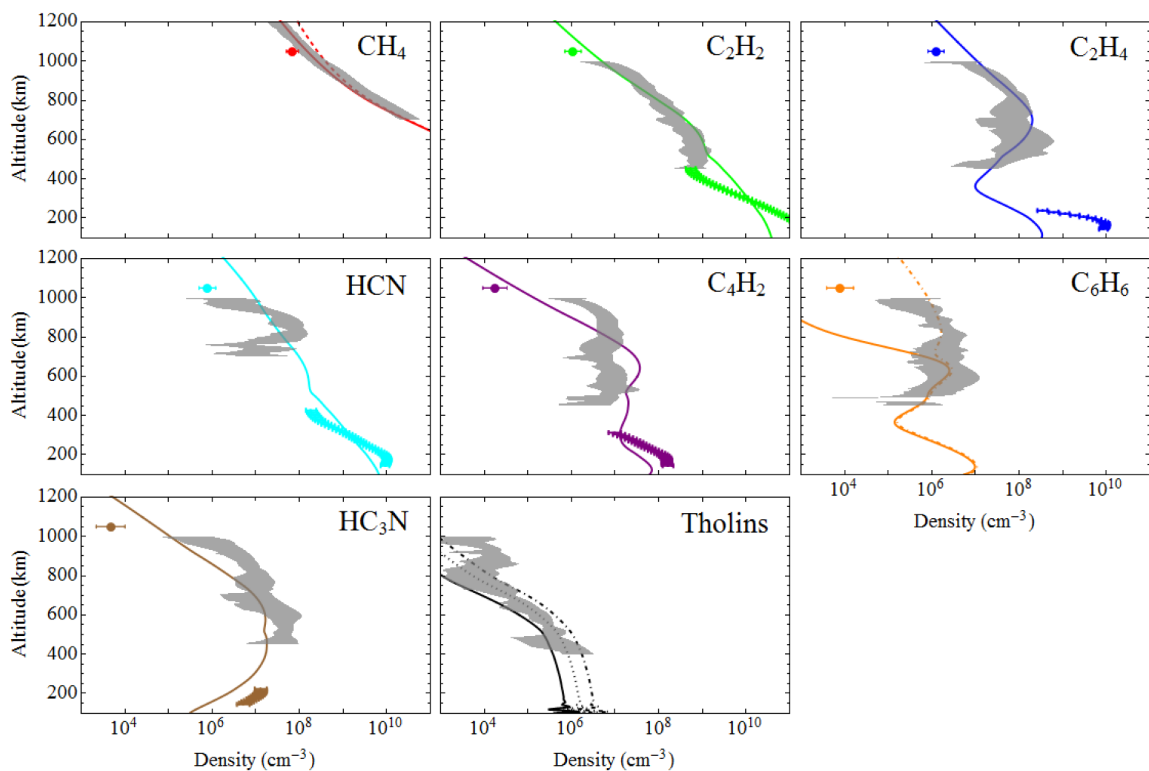


Figure 2.5 : Chemical modeling results are shown above: for CH_4 , both without escape (dashed line), and with escape (solid line); for the rest of the species, only the case with best fit for CH_4 escape is shown (solid line). For C_6H_6 , the improved case with an additional downward molecular flux of $10^8 \text{ cm}^{-2} \text{ s}^{-1}$ is plotted as a dot-dashed line. For tholins, two cases with a downward flux of $1.8 \cdot 10^{-13} \text{ g cm}^{-2} \text{ s}^{-1}$ (dotted line) and $3.6 \cdot 10^{-13} \text{ g cm}^{-2} \text{ s}^{-1}$ (dot-dashed line) are shown. Shaded regions indicate variability of UVIS density retrievals for each species. Also shown for comparison are INMS globally averaged densities at 1050 km (Magee et al., 2009), as well as CIRS data below 400 km (Vinatier et al., 2010).

deposition. A simplified heterogeneous loss scheme is applied for the hydrocarbons above 500 km, with a sticking coefficient of ~ 0.001 . This scheme provides a source of tholins, as well as a sink for the hydrocarbons in order to explain the CIRS measurements below 400 km (Figure 2.5). In addition, a linear chemical loss scheme above 900 km is applied to convert additional C_2 and higher order hydrocarbons into tholins. The loss timescales are assumed to be $2 \cdot 10^6$ s. This scheme is a rather rough approximation, but allows the simulated hydrocarbons to be more consistent with the UVIS and INMS observations. It also simultaneously provides the source of the tholins in the upper atmosphere with a column mass production rate $\sim 4.4 \cdot 10^{-14}$ g cm $^{-2}$ s $^{-1}$, which is about half of that from heterogeneous reactions ($1.1 \cdot 10^{-13}$ g cm $^{-2}$ s $^{-1}$). The tholin profile is shown in Figure 2.5 (solid line). The total mass production rate of tholin is $\sim 1.5 \cdot 10^{-13}$ g cm $^{-2}$ s $^{-1}$ in our model, larger than in previous results (Liang et al., 2007; Lavvas et al., 2009, 2010).

When a similar magnitude of downward tholin flux ($\sim 10^{-13}$ g cm $^{-2}$ s $^{-1}$) is applied at the top boundary, the model results could be in better agreement with observations (Figure 2.5, Tholins, dotted and dot-dashed lines), which implies that there is a source of tholins from ion chemistry in the upper atmosphere and that it is on the same order as from neutral chemistry. The C_6H_6 density from our model is much less than the observations (Figure 2.5, C_6H_6). However, the addition of a downward flux of 10^8 cm $^{-2}$ s $^{-1}$ at the top boundary produces an improved match to the observed data in this region. This also implies an unaccounted source of C_6H_6 in the upper atmosphere, such as production from ion-neutral chemistry.

2.6 Conclusions

The hydrocarbon density retrievals from *Cassini*-UVIS have shed light on a region of Titan's atmosphere that was previously poorly understood. By adjusting our chemical model to match these densities approximately, we can better constrain the atmospheric chemistry on Titan, though it appears a more complete accounting of ion-neutral interaction is needed to explain the observations comprehensively, especially for the observed structure of some hydrocarbons like C_6H_6 . This will be examined in future research, and incoming UVIS occultation data will be processed in order to improve our knowledge of both the spatial and seasonal distribution of hydrocarbons and tholins on Titan.

2.7 Acknowledgements

This research was supported in part by the Cassini UVIS program. DES was supported through Space Environment Technologies. YLY, XZ, and the development of the photochemical model were supported by a NASA PATM grant to the California Institute of Technology. MCL was supported

by an NSC grant 98-2111-M-001-014-MY3 to Academia Sinica.

After this work was completed, we became aware of similar results by Koskinen et al. (2011) using *Cassini*-UVIS data, with an emphasis on physical structure. The inversion techniques used and work done in these two independent investigations are distinct, however, as Koskinen et al. (2011) did not carry out a comparison between the observations and a photochemical model.

Bibliography

- Ajello, J. M., et al. 2007, *Geophysical Research Letters*, 34, L24204
- Ajello, J. M., et al. 2008, *Geophysical Research Letters*, 35, L06102
- Brown, R. H., et al. 2009, *Titan from Cassini-Huygens*, Springer, New York.
- Cabane, M., et al. 1992, *Icarus*, 96, 176
- Coustonis, A. and Taylor, F. 1999, *Titan: The Earth-Like Moon*, World Scientific
- Esposito, L. W., et al. 2004, *Space Science Reviews*, 115, 299
- Esposito, L. W., et al. 2005, *Science*, 307, 1251
- Flasar, F. M., et al. 2005, *Science*, 308, 975
- Khare, B. N., et al. 1984, *Icarus*, 60, 127
- Koskinen, T., et al. 2011, *Icarus*, 216, 507
- Krasnopolsky, V. A. 2009, *Icarus*, 201, 226
- Lavvas, P. P., et al. 2008, *Planetary and Space Science*, 56, 27
- Lavvas, P. P., et al. 2009, *Icarus*, 201, 626
- Lavvas, P. P., et al. 2010, *Icarus*, 210, 832
- Liang, M., et al. 2007, *The Astrophysical Journal Letters*, 661, L199
- Lunine, J. 2005, *Astrobiology: A Multi-Disciplinary Approach*, Pearson Addison-Wesley
- Magee, B., et al. 2009, *Planetary and Space Science*, 57, 1895
- Moses, J. I., et al. 2000, *Icarus*, 143, 244
- Rodgers, C. 2000, *Inverse Methods for Atmospheric Sounding*, World Scientific
- Shemansky, D. E., et al. 2005, *Science*, 308, 978

- Smith, G., et al. 1982, *Journal of Geophysical Research*, 87, 1351
- Strobel, D. F. 1982, *Planetary and Space Science*, 30, 839
- Vervack, R. J., et al. 2004, *Icarus*, 170, 91
- Vinatier, S., et al. 2010, *Icarus*, 205, 559
- Waite, J. H., et al. 2005, *Science*, 308, 982
- Wilson, E. and Atreya, S. 2003, *Planetary and Space Science*, 51, 1017
- Yelle, R., et al. 2006, *Icarus*, 182, 567
- Yelle, R., et al. 2008, *Journal of Geophysical Research*, 113, E10003
- Yung, Y. L. 1987, *Icarus*, 72, 468
- Yung, Y. L., et al. 1984, *The Astrophysical Journal Supplement Series*, 55, 465

Chapter 3

Composition of Titan's Upper Atmosphere from Cassini UVIS EUV Stellar Occultations

Originally published as:

Kammer, J. A., et al. 2013, Planetary and Space Science, 88, 86

3.1 Summary

Identifying seasonal and spatial variability in Titan's atmospheric structure is a key factor in improving theoretical models of atmospheric loss and understanding the physical processes that control the loss rate. In this work, the extreme ultraviolet (EUV) stellar occultation lightcurves from the Cassini Ultraviolet Imaging Spectrograph (UVIS) experiment are analyzed. N_2 and CH_4 atmospheric profiles between 1000 and 1400 km are determined by using an optimized grid search retrieval method to provide a complete χ^2 surface for the two species abundance parameters at each level in the atmosphere. Kinetic temperature is extracted from hydrostatic analysis of the N_2 profiles, and indicates a high level of variability related to energy deposition in the upper atmosphere. These results are compared to *in situ* measurements by the Ion Neutral Mass Spectrometer (INMS), which also probes this region of Titan's atmosphere.

3.2 Introduction

The stellar and solar occultations at Titan using the *Cassini* UVIS experiment provide measurements of the vertical profiles of chemical species over an altitude range of 400 km to above 1500 km. The published results to date (Shemansky et al., 2005; Liang et al., 2007a; Koskinen et al., 2011) have provided vertical profiles obtained from selected occultations. These results are used to constrain

rates of chemical production and dynamics in atmospheric models. Titan’s atmosphere is of particular interest because for a small planetary body it has a significant mass, with a surface pressure 1.5 times that of Earth, but with an inferred loss rate because of low gravity (Hunten, 1982; Yelle et al., 2008; Strobel, 2009; Bell et al., 2010, 2011; Mandt et al., 2012). A thorough characterization of the chemical composition and physical properties of Titan’s upper atmosphere is highly desirable both to utilize it as a natural laboratory for understanding low temperature, low pressure chemical reaction rates and mechanisms, as well as to trace the forcing of Titan’s seasonal variability.

Modeling the complex suite of reactions that occur in such an atmospheric system is currently an area of active research (Yung et al., 1984; Yung, 1987; Lavvas et al., 2008a, 2011a; Krasnopolsky, 2009). Aerosols are an important end product of Titan’s atmospheric chemistry, and much effort has gone into modeling their formation (Cabane et al., 1992; Wilson and Atreya, 2003; Liang et al., 2007a; Lavvas et al., 2009, 2010, 2011b). These models improve as observations constrain the spatial and seasonal changes in Titan’s atmosphere. Along with the *Cassini* INMS and VIMS experiments (Yelle et al., 2006; García-Comas et al., 2011), the Ultraviolet Imaging Spectrograph (UVIS) has the capability of probing the region where much of the chemistry driven by solar and magnetospheric input on Titan occurs. UVIS observations of emission from N_2 airglow have been examined previously (Ajello et al., 2007, 2008; Stevens et al., 2011). Solar occultation observations in the EUV using UVIS have also been analyzed (Capalbo et al., 2013). The stellar occultation analysis has to date been restricted to measurement of the hydrocarbon components, because sufficiently accurate N_2 cross sections have not been available until the last few years (Liang et al., 2007b). This paper provides measurements of N_2 and CH_4 by the UVIS extreme ultraviolet (EUV) spectrograph, obtained for the first time utilizing stellar occultation observations from *Cassini*.

Details of the instrument and of instrumental effects on observations are discussed in §3.3. Previous work (Shemansky et al., 2005; Liang et al., 2007a; Koskinen et al., 2011) has examined stellar occultation lightcurves in the far ultraviolet (FUV) region of the spectrum, revealing density profiles for hydrocarbons including CH_4 , C_2H_2 , C_2H_4 , C_4H_2 , C_6H_6 , HCN, HC_3N , and tholins. In this work, the extreme ultraviolet (EUV) lightcurves are analyzed to determine the densities of the two dominant species in Titan’s atmosphere, N_2 and CH_4 . Kinetic temperature of the upper atmosphere is extracted from hydrostatic analysis of the N_2 profiles. The retrieval methodology used to derive these quantities is described in §3.4, and the results, along with comparison to results from the *Cassini* Ion Neutral Mass Spectrometer (INMS), are discussed in §3.5. Conclusions are summarized in §3.6.

3.3 The UVIS Instrument

3.3.1 FUV and EUV Spectrographs

A full description of the UVIS experiment is contained in Esposito et al. (2004), but the relevant components of interest for this work are the EUV and FUV spectrographs. The spectral range of the spectrographs is 563 - 1182Å (EUV) and 1115 - 1912Å (FUV); these spectral regions provide complementary atmospheric composition information during simultaneous exposure. Stellar flux in the FUV region generally can be detected down to observation tangent heights of about 400 km, revealing the profiles of a wide range of hydrocarbons, including CH₄, C₂H₂, C₂H₄, C₄H₂, C₆H₆, HCN, HC₃N, and tholins. On the other hand, EUV stellar flux is largely absorbed at tangent heights of about 1000 km; however, observations in the EUV present the unique opportunity to study N₂, which does not have absorption features in the FUV. The ionization continuum of methane in the EUV allows extraction of the CH₄ profile.

3.3.2 Instrument Model

Details for modeling of species abundances from the UVIS measurements are described by Shemansky et al. (2005) and Shemansky and Liu (2012). The absorption spectra are forward modeled using a high resolution blanketed model of the stellar source with simulation of the instrument response to the source spectrum. The simulation process includes analytic functions matching the wavelength dependent point spread functions (psf) that characterize the spectrographs. The stellar model and simulation process are also described in Chapter 9 of the *Cassini* UVIS Users Guide (2012), available in the NASA PDS. Examples of the impact of the psf on the analysis are given by Shemansky et al. (2005); Liang et al. (2007a); Shemansky and Liu (2012). In the present work the filtered raw data is used to produce the extinction profiles. The mechanics of the occultation process in the Cassini spacecraft system are described in the supporting online material of Shemansky et al. (2005). High resolution photoabsorption cross sections for the N₂X(0) state at a temperature of 150 K were obtained from coupled channel calculations by A. N. Heays and B. R. Lewis (Liang et al., 2007b). These cross sections were obtained with a resolving power of $\sim 10^6$ at increments of 1 cm^{-1} . CH₄ cross sections used in the reduction process are taken from Kameta et al. (2002).

3.3.3 Spacecraft Pointing Issues

The accuracy of the extinction spectrum in occultation observations, apart from photon counting statistics, is limited by the stability of instrument pointing. Normally the spacecraft reaction wheels retain pointing well within the limits required for accurate spectral records. During flybys of Titan, however, transitions are necessary between thruster and reaction wheel control, and observations may

Table 3.1. Analyzed Stellar Occultations

Titan Flyby	Date (Year-Day)	Stellar Target	Latitude	Longitude	Log N_0 (cm^{-3}) ^a	T (K) ^b
T21	2006-346	α Eri	35 S	116 W	$20.17^{+0.90}_{-0.90}$	$149.6^{+13.6}_{-11.6}$
T35	2007-243	σ Sgr	35 S	329 W	$16.47^{+0.96}_{-0.69}$	$225.0^{+25.0}_{-26.5}$
T41-I	2008-054	ϵ CMa	4 S	333 W	$20.81^{+0.86}_{-0.82}$	$136.9^{+10.1}_{-9.7}$
T41-II	2008-054	ϵ CMa	24 S	173 W	$21.86^{+0.96}_{-0.98}$	$124.8^{+10.1}_{-8.8}$

^aBest-fit parameterized density from model calculations.

^bBest-fit parameterized temperature from model calculations.

occur in a transition period, introducing instability in the position of the image on the detector. These events significantly affect the process of obtaining accurate extinction spectra. While it may yet be possible to correct for these shifts in flux, the effects are highly nonlinear, and thus the initial analysis of occultation data is limited to cases where little or no pointing issues occur. These cases are presented below in §3.3.4.

3.3.4 Occultation Spatial/Seasonal Coverage

Over 20 Titan stellar occultation events were observed by the EUV spectrograph from 2004 through 2010; of these, there are four stellar occultations during Titan flybys T21, T35, and T41 that present stable observations. The details of these occultations are shown in the first part of Table 3.1. The occultation latitude and longitude is determined based on the projection of observation geometry for tangent heights (impact parameter) between 1000 and 1400 km; in this region these projected values vary less than 1-2 degrees due to trajectory motion during the course of the observation.

3.4 Methodology

3.4.1 Forward Model

In order to retrieve the abundances of N_2 and CH_4 from each spectrum that UVIS records during an observation, a forward model is constructed that utilizes the species cross sections in the EUV. This model simulates the instrument response to a calculated extinction spectrum of the transmitted stellar source model through a model atmosphere, as described in §3.3.2.

The generation of a reference database allows for fast and efficient forward modeling of species abundances (η_s) to optical depth (τ_λ) in the EUV. In this case, the database includes a tabulated grid of values for both N_2 and CH_4 , at 50 line of sight abundances ranging from $\eta = 10^{14}$ to 10^{19} cm^{-2} , and 512 wavelength values corresponding to the UVIS windowed EUV mode ($\lambda = 870\text{\AA}$ to 1180\AA). This database is represented by:

$$\tau_\lambda = \tau_\lambda(\eta_{\text{N}_2}, \eta_{\text{CH}_4}) \quad (3.1)$$

A spectrum corresponding to the clear atmosphere view of the target star is obtained from instrument observations taken above an impact parameter of 1800 km. This I_0 spectrum completes the forward model in Equation 3.2:

$$I_\lambda = I_{0,\lambda} \exp(-\tau_\lambda) \quad (3.2)$$

Statistical uncertainty in the I_0 spectrum is determined by calculating the standard deviation at each wavelength of the observations made above 1800 km. Figure 3.1 shows an example of the I_0 spectrum and the standard deviation for Titan flyby T41-I during the occultation of the star ϵ CMa, as well as a sample spectrum taken deeper into the atmosphere.

3.4.2 Retrieval Algorithm

In a multivariate system with a forward model containing many independent parameters, it becomes computationally infeasible to conduct a brute force grid search in order to determine the marginalized posterior likelihoods for each variable in a χ^2 sense. Such is the case for previous examinations of UVIS spectra in the FUV (Koskinen et al., 2011); in order to simultaneously fit for many different hydrocarbon species, a Levenberg-Marquardt routine was adopted similar to that of Rodgers (Rodgers, 2000). This routine and similar ones take advantage of the assumption of Gaussian parameter uncertainties in order to speed up calculations, and in general provide the fastest retrieval. Other statistical studies have also experimented with the use of Markov Chain Monte Carlo (MCMC) algorithms and their derivatives (Andrieu et al., 2003), which can be computationally intensive but are beneficial in situations where an assumption of Gaussian uncertainties is invalid.

For this work there are only two parameters adjusted in the forward model: η_{N_2} and η_{CH_4} . This computational advantage, combined with a highly parallelized grid search retrieval code, allows for a complete determination of the two parameter χ^2 surface for combinations of N_2 and CH_4 abundances at each level in the atmosphere. This avoids making any assumptions about the shape of parameter uncertainties, and is therefore a more robust method for estimating the uncertainty in retrieved column densities than assuming Gaussian errors. An example of a retrieved reduced χ^2 contour map is shown in Figure 3.2. Reduced χ^2 is equivalent to χ^2/ν , where ν is the number of degrees of freedom, given as $N - n$, where N is the number of data points and n is the number of fitted model parameters. In this case, $N = 512$ and $n = 2$, thus $\nu = 510$.

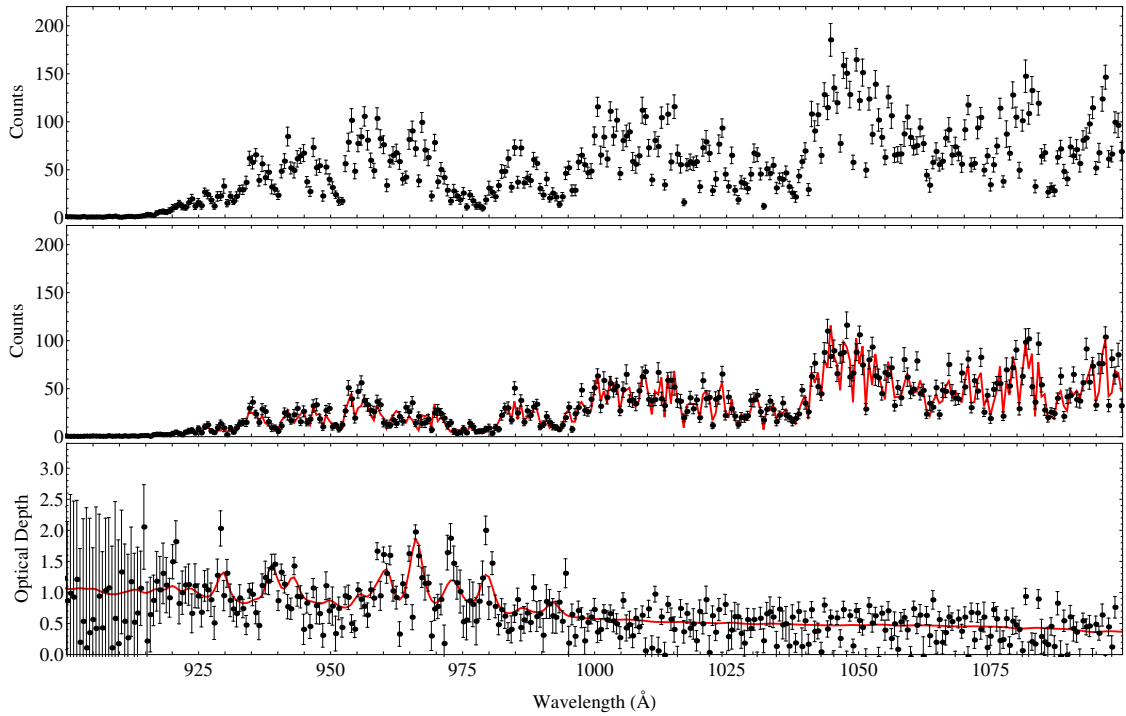


Figure 3.1 : Intensity and optical depth spectra during occultation T41-I. The top panel shows the I_0 stellar flux, taken as the median of all 5-second integrated records at tangent heights above 1800 km. Error bars are the associated standard deviation of the flux. The middle panel shows the equivalent spectrum at a height of 1092 km, with stellar flux (black) compared to the best fit model (red). The bottom panel provides the same comparison using optical depth units.

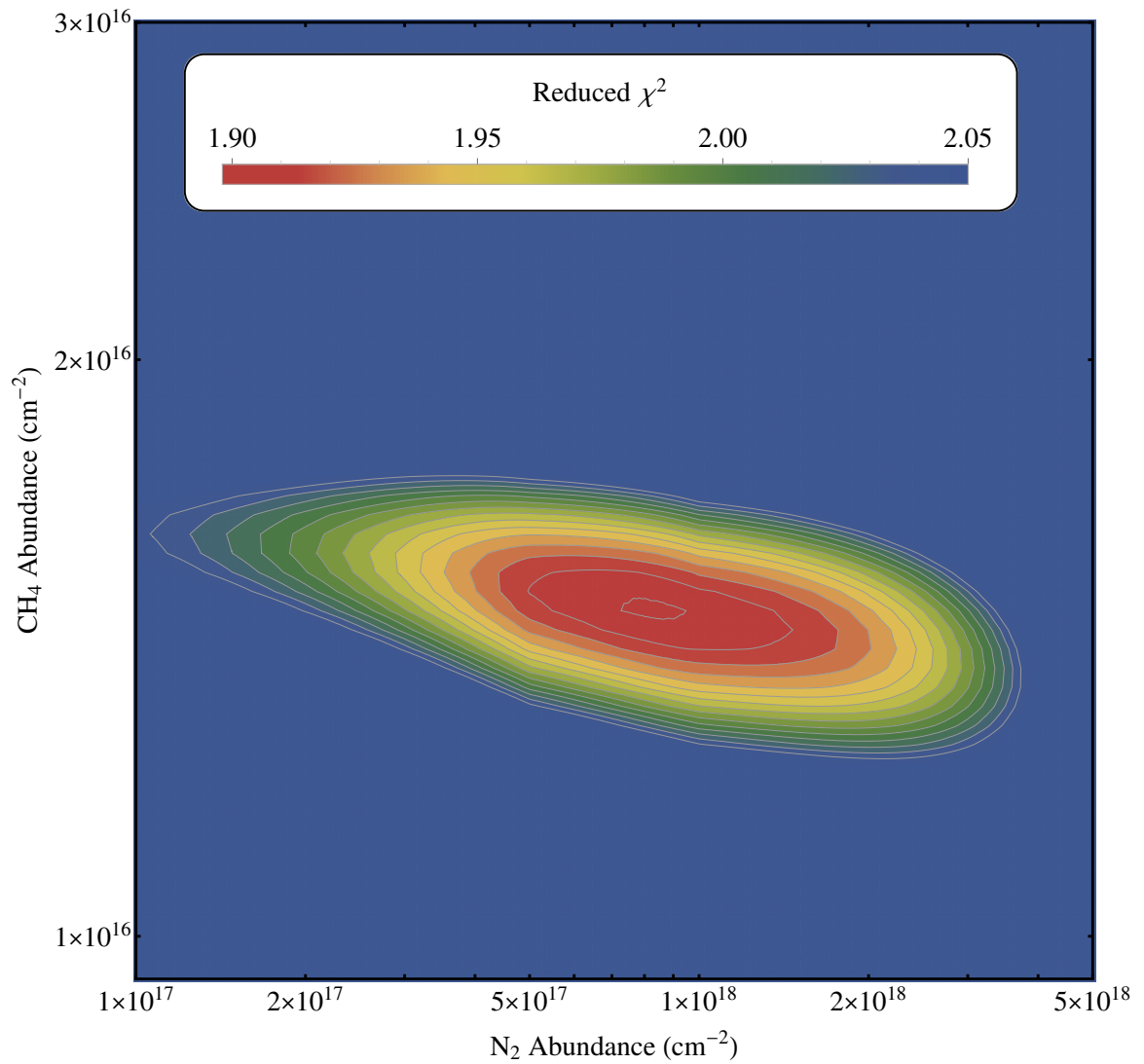


Figure 3.2 : Contour map showing an example of the two parameter grid search method used to determine the reduced χ^2 surface. Grid resolution for each parameter is 0.01 in log abundance space. This fit is for flyby T41-I at an occultation tangent height of 1092 km. The process is repeated for each tangent height made during the observation.

3.4.3 Conversion from Abundance to Density Profiles

Once the χ^2 surface has been calculated, the marginalized posterior likelihoods for each parameter can be obtained by projecting the total χ^2 along each parameter axis. Several examples of these marginalized posteriors at different heights are shown in Figure 3.3. These distributions are then used to calculate the best fit pair of parameters, along with their corresponding 1σ uncertainties.

Though approximately Gaussian in shape, the N_2 posterior probability distributions are asymmetric near the top and bottom of the observation region. Above about 1500 km, there is only enough absorption to provide upper limit constraints; likewise, as tangent heights of 1000 km are reached, too few EUV photons remain to constrain N_2 .

The initial retrieved values, in physical terms, are line of sight column abundances - an example of a full profile of N_2 and CH_4 abundances is shown in Figure 3.4. In order to make the conversion from abundances to densities, spherical symmetry of the atmosphere is assumed such that the well-known inverse Abel transform may be applied, as in Equation 3.3:

$$\rho(r) = -\frac{1}{\pi} \int_r^\infty \frac{d\eta}{dh} \frac{dh}{\sqrt{h^2 - r^2}} \quad (3.3)$$

In this case, $\rho(r)$ is the local density as a function of the distance from Titan's center, r ; $\eta(h)$ is the retrieved line of sight abundance as a function of the tangent height, h , also calculated as distance from Titan's center. The limits of integration extend to infinity, but the UVIS measurements generally only begin or end at tangent heights of approximately 2000 km or so above the surface of Titan; a method of extrapolation is needed to account for the unobserved atmosphere above this region, therefore a simple exponential decrease with altitude is fit to the observed data. It should be noted that the sensitivity of the retrieved density profiles to this extrapolation region is minimal, and its use is primarily to avoid nonphysical solutions.

The species density uncertainties at each altitude are determined using a series of 1000 random draws from the abundance posterior distributions in order to propagate the calculated parameter uncertainties. This creates a set of 1000 density profiles, which represent at each altitude the propagated uncertainty in species density. The median of this distribution is taken as the best fit solution, and the 68% confidence interval represents the 1σ uncertainty. An example of the resulting profile, including the best fit densities and their 1σ uncertainties, is shown in Figure 3.5.

3.4.4 Effective Temperatures from Fits to N_2 Scale Height

In addition to retrieved atmospheric composition in terms of N_2 and CH_4 densities, the effective temperature of this region of Titan's atmosphere can also be determined assuming a constant scale height, H_s , with altitude. This is essentially identical to a procedure performed using *Cassini* Ion

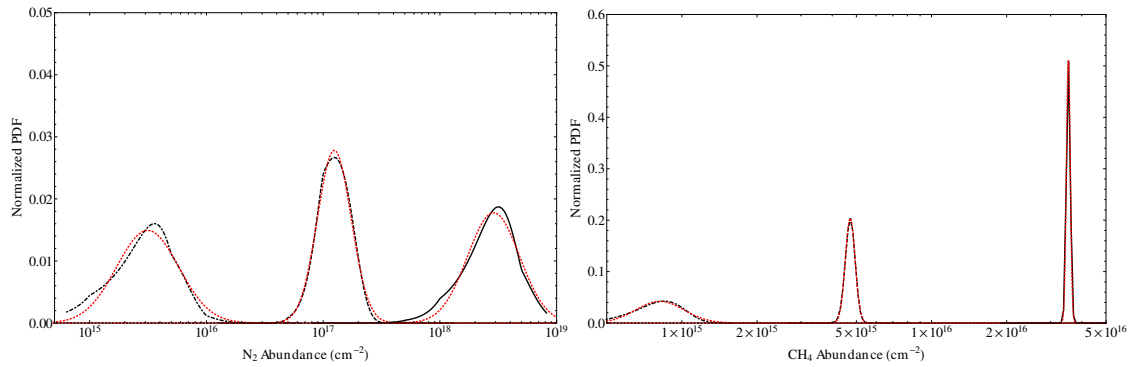


Figure 3.3 : Comparison between tangent heights. Shown are the marginalized posterior likelihood distributions (black) for the abundances of both N_2 and CH_4 during occultation T41-I. The three curves correspond to three different levels in Titan's atmosphere: 1457 km (dash-dotted line, left), 1193 km (dashed line, middle), and 1010 km (solid line, right). The red, dotted curves are best fit Gaussian distributions in log space.

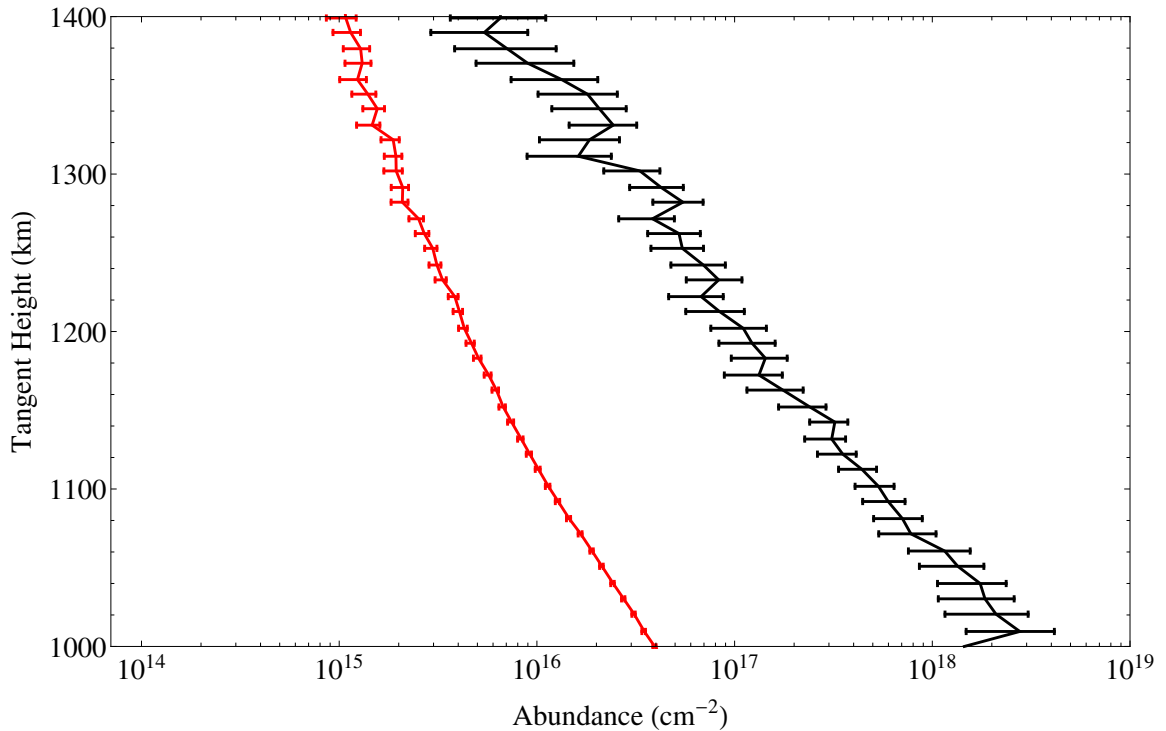


Figure 3.4 : Retrieved line of sight abundances. Shown here is the profile of N_2 (black) and CH_4 (red) for occultation during T41-I. Methane abundances are highly constrained, while nitrogen is less so.

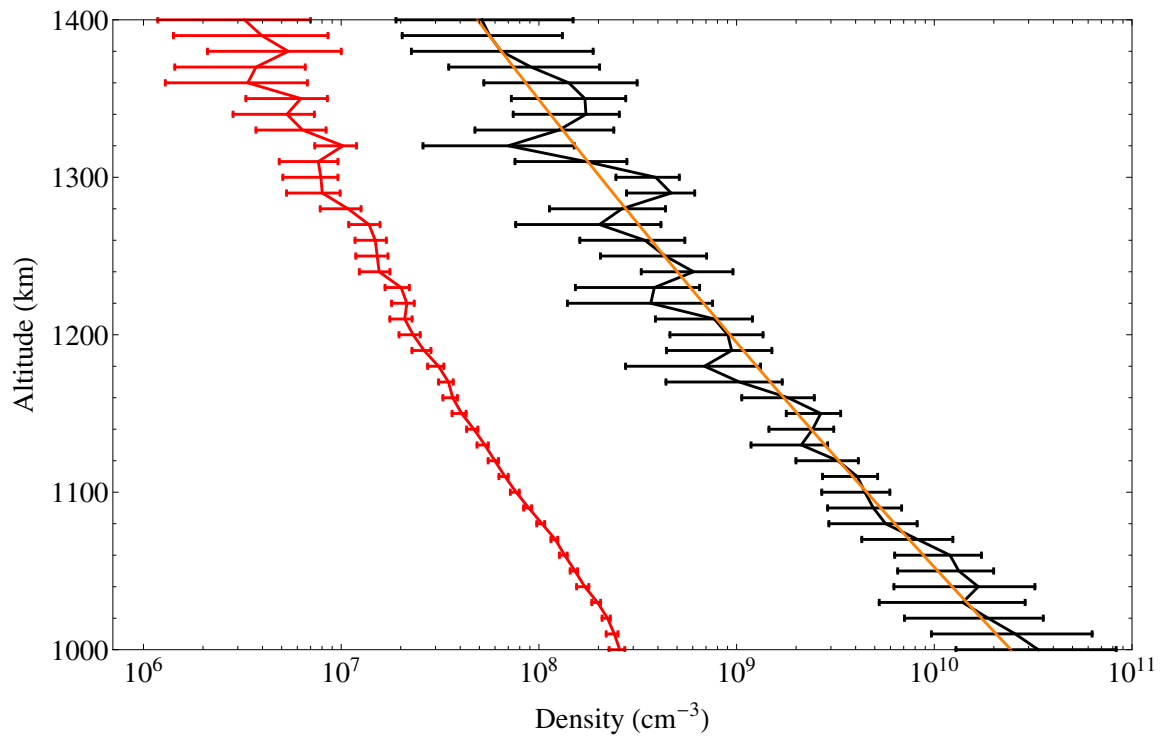


Figure 3.5 : Calculated species density profiles and isothermal fit. Density is determined from the retrieved line of sight abundances using the inverse Abel transform of Equation 3.3. Here again, the best fit N₂ profile is shown in black, with the associated 1 σ uncertainty; corresponding profiles for CH₄ are shown in red. The isothermal, hydrostatic model (orange) is fit to N₂ density and used to calculate the effective temperature in this region of Titan's upper atmosphere.

Neutral Mass Spectrometer (INMS) data by Westlake et al. (2011). Because the effect of gravity cannot be assumed constant in this region of Titan’s atmosphere, the altitude used in the scale height fit is replaced with a surface referenced geopotential height, simplifying the calculation. Thus,

$$z = \frac{h}{1 + h/R_{Titan}} \quad (3.4)$$

$$H_s = \frac{kT_{eff}}{m_s g_0} \quad (3.5)$$

$$N_s(z) = N_{s,0} \exp(-z/H_s) \quad (3.6)$$

In Equation 3.4, z is geopotential height, h is altitude, and R_{Titan} is the radius of Titan. In Equation 3.5, the scale height H_s is determined by k , Boltzmann’s constant; T_{eff} , the effective temperature; m_s , the mass of species s ; and g_0 , the gravitational acceleration at the surface of Titan. Lastly, in Equation 3.6, the species number density N_s as a function of geopotential height is assumed hydrostatic and isothermal with a parametrized surface number density $N_{s,0}$, allowed to vary in the fit. An example of the model fit to the data is also shown in Figure 3.5.

3.5 Results and Discussion

3.5.1 Retrieved Abundance and Density Profiles

The results of analysis for all stellar occultations examined in this work are shown in Figure 3.6. The abundances and their marginalized posterior likelihood distributions are used directly to calculate local densities at each altitude level between 1000 and 1400 km. While global coverage of UVIS EUV occultation data sets is relatively limited, results from measurements by *Cassini* INMS have revealed *in situ* densities for 29 Titan flybys (Westlake et al., 2011). This allows for density retrievals from UVIS to be understood in a broader context. For instance, even among a small number of UVIS observations, there appears to be a significant amount of variability in the density profiles; such variability is also strongly indicated in the INMS data (Cui et al., 2009, 2012; Magee et al., 2009; Westlake et al., 2011). Figure 3.7 shows the comparison between this work and the collective results from 29 flybys of INMS.

3.5.2 Effective Temperatures

Model fits of isothermal, hydrostatic nitrogen profiles for each stellar occultation examined in this work are also shown in Figure 6. Effective temperatures and their uncertainties are shown in the second part of Table 3.1. While too few in number to examine any possible correlation with plasma

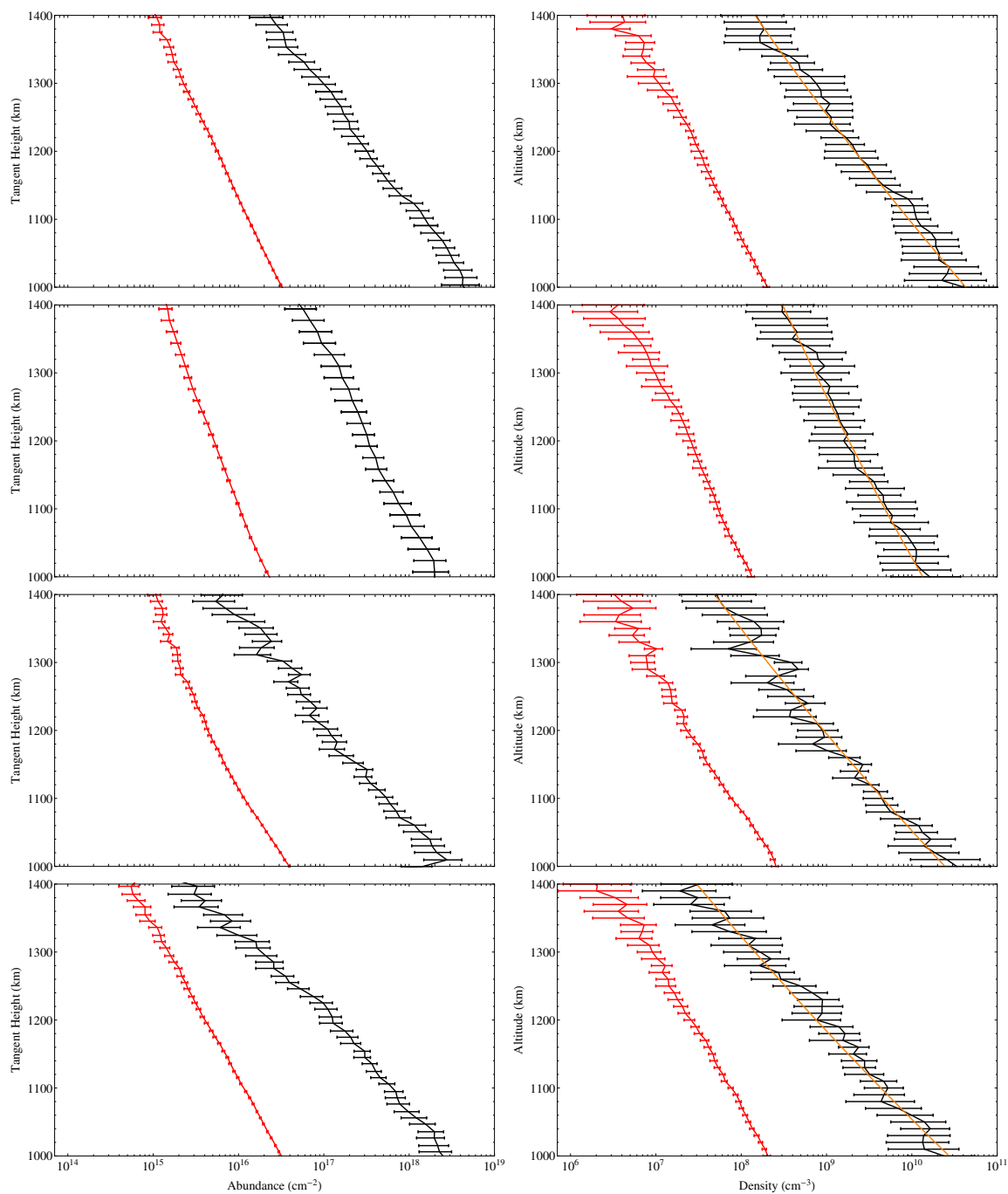


Figure 3.6 : Ensemble of results for each occultation. Retrieved line of sight abundances, calculated densities for N_2 (black) and CH_4 (red), and isothermal model fits (orange) for Titan flybys T21, T35, T41-I, and T41-II (in rows 1-4, respectively).

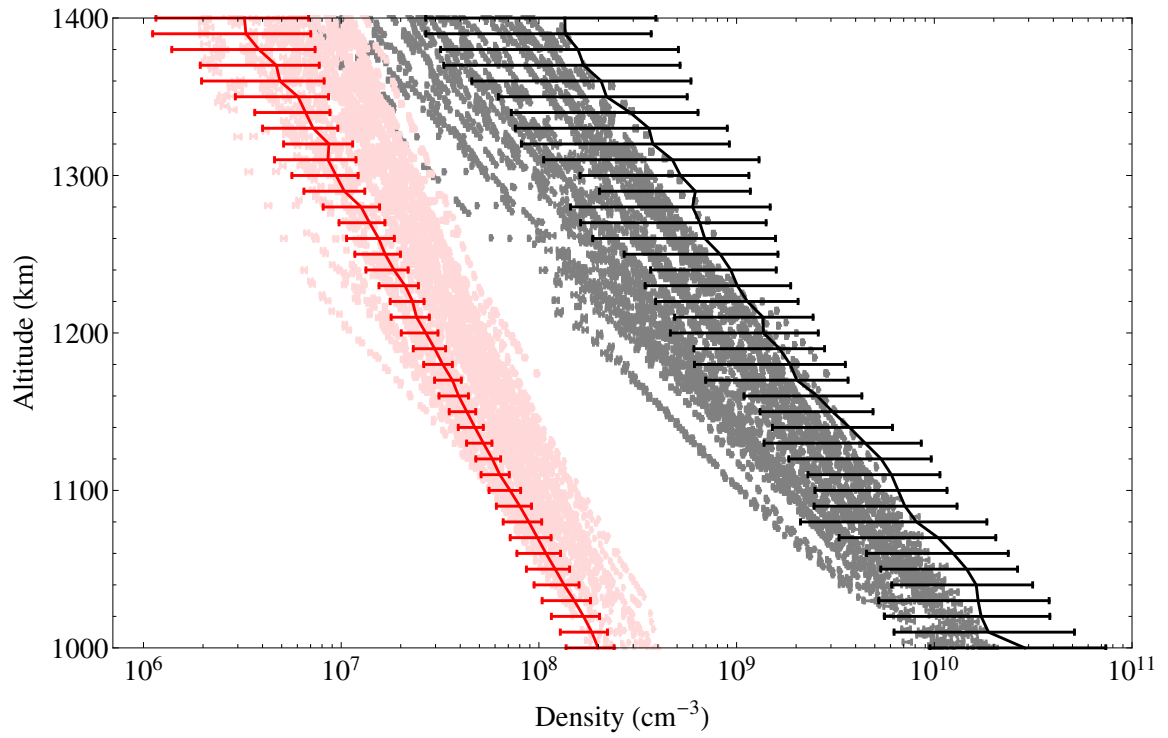


Figure 3.7 : Comparison with INMS results. Plotted are the mean values of the four N_2 (black) and CH_4 (red) density profiles retrieved from the stellar occultation examined in this work, along with their associated range of uncertainties. Density profiles for N_2 and CH_4 from 29 flybys of INMS are shown in gray and light red, respectively (Westlake et al., 2011).

environments as in Westlake et al. (2011), the UVIS results still show significant variability, including an effective temperature difference of nearly 100 K between flybys T35 and T41. It is important to note, however, that while this effective temperature calculation reveals trends for the upper atmosphere as a whole, temperature cannot be constant starting at 1000 km; this is the location of the ionospheric peak where the heating profile has a large slope. Future work is needed to extract non-isothermal temperature profiles.

3.6 Conclusions

Stellar occultation observations from *Cassini* UVIS have confirmed Titan's upper atmosphere to be a dynamic environment. Analysis of data from the instrument's EUV spectrograph complement those previously derived from the FUV, and provide context for the bulk atmospheric properties of the upper atmosphere. Though limited by the effect of pointing instability, a select number of occultation measurements allow for additional constraints to be made on the profiles of N_2 and CH_4 , as well as on the effective temperatures of the upper atmosphere between 1000 and 1400 km. The results show that even averaged over thousands of kilometers, the column N_2 and CH_4 exhibit large variabilities. The apparent changes observed in these physical parameters may indicate spatial and seasonal differences in the deposition of energy, perhaps driven by magnetospheric input as previously suggested by Westlake et al. (2011) using *in situ* results from INMS.

3.7 Acknowledgements

This research was supported in part by the *Cassini* UVIS program via NASA grant JPL.1459109 to the California Institute of Technology. YLY and XZ were supported in part by NASA grant NNX09AB72G to the California Institute of Technology. DES was supported through Space Environment Technologies. JAK would like to thank Michael Line for many productive discussions concerning data analysis and retrieval methodology, as well as Joseph Westlake for assistance in providing INMS derived nitrogen and methane atmospheric profiles.

Bibliography

- Ajello, J. M., et al. 2007, *Geophysical Research Letters*, 34, L24204
- Ajello, J. M., et al. 2008, *Geophysical Research Letters*, 35, L06102
- Andrieu, C., et al. 2003, *Machine Learning*, 50, 5
- Bell, J. M., et al. 2010, *Journal of Geophysical Research: Planets*, 115, E12002
- Bell, J. M., et al. 2011, *Journal of Geophysical Research: Planets*, 116, E11002
- Cabane, M., et al. 1992, *Icarus*, 96, 176
- Capalbo, F. J., et al. 2013, *The Astrophysical Journal Letters*, 766, L16
- Chen, F., and Wu, C. 2004, *Journal of Quantitative Spectroscopy and Radiative Transfer*, 85, 195
- Coustenis, A., and Taylor, F. 1999, *Titan: The Earth-like Moon*, World Scientific
- Cui, J., et al. 2009, *Icarus*, 200, 581
- Cui, J., et al. 2012, *Journal of Geophysical Research: Planets*, 117, E11006
- Esposito, L., et al. 2004, *The Cassini-Huygens Mission*, 299
- Esposito, L., et al. 2005, *Science*, 307, 1251
- Flasar, F., et al. 2005, *Science*, 308, 975
- García-Comas, M., et al. 2011, *Icarus*, 214, 571
- Hunten, D. M. 1982, *Planetary and Space Science*, 30, 773
- Kameta, K., et al. 2002, *Journal of Electron Spectroscopy and Related Phenomena*, 123, 225
- Koskinen, T., et al. 2011, *Icarus*, 216, 507
- Krasnopolsky, V. 2009, *Icarus*, 201, 226
- Lavvas, P., et al. 2008, *Planetary and Space Science*, 56, 27

- Lavvas, P., et al. 2009, *Icarus*, 201, 626
- Lavvas, P., et al. 2010, *Icarus*, 210, 832
- Lavvas, P., et al. 2011a, *Icarus*, 213, 233
- Lavvas, P., et al. 2011b, *The Astrophysical Journal*, 728, 80
- Lewis, B., et al. 2008, *The Journal of Chemical Physics*, 129, 164305
- Liang, M., et al. 2007a, *The Astrophysical Journal Letters*, 661, L199
- Liang, M., et al. 2007b, *The Astrophysical Journal Letters*, 664, L115
- Lunine, J. 2005, *Astrobiology: A Multi-Disciplinary Approach*, Pearson Addison-Wesley
- Lunine, J., et al. 2009, *Titan from Cassini-Huygens*, 35
- Magee, B., et al. 2009, *Planetary and Space Science*, 57, 1895
- Mandt, K. E., et al. 2012, *The Astrophysical Journal*, 749, 160
- Moses, J. I., et al. 2000, *Icarus*, 143, 244
- NASA-PDS 2012, *Cassini UVIS User's Guide*,
Planetary Data System - <http://pds-rings.seti.org/cassini/uvis/index.html>
- Rodgers, C. 2000, *Inverse Methods for Atmospheric Sounding*, World Scientific
- Shemansky, D., et al. 2005, *Science*, 308, 978
- Shemansky, D., and Liu, X. 2012, *Canadian Journal of Physics*, 90, 817
- Smith, G., et al. 1982, *Journal of Geophysical Research*, 87, 1351
- Stevens, M., et al. 2011, *Journal of Geophysical Research*, 116, A05304
- Strobel, D., 2009, *Icarus*, 202, 632
- Vinatier, S., et al. 2007, *Icarus*, 188, 120
- Vinatier, S., et al. 2010, *Icarus*, 205, 559
- Westlake, J., et al. 2011, *Journal of Geophysical Research*, 116, A03318
- Wilson, E. and Atreya, S. 2003, *Planetary and Space Science*, 51, 1017
- Yelle, R. 1991, *The Astrophysical Journal*, 383, 380
- Yelle, R., et al. 2006, *Icarus*, 182, 567

Yelle, R., et al. 2008, *Journal of Geophysical Research*, 113, E10003

Yung, Y. L. 1987, *Icarus*, 72, 468

Yung, Y. L., et al. 1984, *The Astrophysical Journal Supplement Series*, 55, 465

Chapter 4

Atmospheric Profiles of Titan's High-Altitude Haze: *Cassini* UVIS Stellar Occultation Measurements

4.1 Summary

We present retrievals of Titan haze optical properties derived from *Cassini* UVIS stellar occultation observations of the upper atmosphere above 300 km. These measurements focus on the wavelength region in the far ultraviolet (FUV) between 1850 - 1900Å, where absorption by other hydrocarbon species is minimal. While this work does not uniquely estimate haze particle absorptivity and number density separately, we provide robust estimates of the combined effects of these two physical parameters over multiple Titan flybys. The results provide valuable constraints for models of Titan haze formation throughout this region of the upper atmosphere.

4.2 Introduction

Our understanding of the chemical composition and dynamics of Titan's atmosphere has advanced dramatically since the *Cassini* spacecraft entered orbit around Saturn in 2004. Perhaps one of the more challenging areas of research, however, has centered around the characterization of Titan tholins, one of the major end products of ion and neutral chemistry in Titan's upper atmosphere. Titan aerosol analogs have been created and measured in the laboratory (Khare et al., 1984; Thissen et al., 2009; Cable et al., 2012; Hörst and Tolbert, 2013; Yoon et al., 2014), and this approach has led to better understanding of formation precursors and mechanisms, though it remains difficult to entirely replicate the environmental conditions present at Titan. Computational models of both the chemical and physical state of Titan's atmosphere have also improved our knowledge of aerosol formation (Krasnopolsky, 2009; Lavvas et al., 2008a,b, 2010, 2011a,b, 2013). Both laboratory and

computational approaches require observational evidence in order to convince ourselves of their accuracy, however. *Cassini* has provided a wealth of resources in this regard, and this work builds on previous efforts to provide valuable constraints on the presence and properties of aerosols in Titan’s upper atmosphere.

Ion production and chemistry plays an important role in initial aerosol formation (Dutuit et al., 2013), and *in situ* measurements by the *Cassini* Ion Neutral Mass Spectrometer (INMS) have revealed much about the starting material for Titan tholin formation (Vuitton et al., 2007, 2008, 2009; Mandt et al., 2012). These measurements are limited to the atmospheric region above about 850 km, where the *Cassini* spacecraft makes its closest flybys. Remote sensing instruments are required to probe the region of the atmosphere below this point, and the Ultraviolet Imaging Spectrograph (UVIS) in particular excels at this task. Previous work has utilized solar and stellar occultation observations with UVIS to detect a wide range of Titan’s chemical species, including N₂, CH₄, other minor hydrocarbons, and aerosols (Shemansky et al., 2005; Liang et al., 2007; Koskinen et al., 2011; Capalbo et al., 2013; Kammer et al., 2013). The results of Koskinen et al. (2011) also confirmed the apparent collapse of the detached haze layer on Titan (Lavvas et al., 2009; West et al., 2011).

This work provides a deeper look at a full range of 13 stellar occultation observations from T21 to T58. We derive profiles of aerosol attenuation coefficients (α , km⁻¹) for the atmospheric region between 300 - 900 km at a range of latitudes. §4.3 goes into greater detail on the available datasets and selection criteria, while §4.4 describes the data processing and reduction methodology. Discussion of the implications of these results and their impact on future work is found in §4.5 and §4.6, respectively.

4.3 *Cassini* UVIS Stellar Occultation Observations

4.3.1 Titan Flybys

The work of Koskinen et al. (2011) went into detail for two Titan flybys, T41 and T53. They obtained estimates for the height of the detached haze layer for several others, but did not provide full profile retrievals for these additional observations. We revisit the datasets in this work, covering a temporal and spatial range as listed in Table 4.1. Pointing stability has been an issue for many of these observations, as pointing drift and oscillations can result in non-linear shifts in the observed spectrum on the detector array. In this work we are able to analyze many of the previously unusable datasets due to a focused selection of FUV wavelengths where aerosols are predominantly responsible for absorption.

Table 4.1. Titan Stellar Occultations

Flyby	UT Start Date	Stellar target	Latitude	Longitude
T21	2006-12-12	α Eri	35 S	116 W
T23	2007-01-13	η UMa	4 S	232 W
T35	2007-08-31	σ Sgr	33 S	328 W
T40	2008-01-05	α Lyr	53 N	33 W
T41-I	2008-02-23	ϵ CMa	8 S	332 W
T41-II	2008-02-23	ϵ CMa	27 S	175 W
T47-I	2008-11-19	η Uma	1 N	24 W
T47-II	2008-11-19	β CMa	55 N	340 W
T48	2008-12-05	ϵ CMa	19 N	320 W
T52	2009-04-03	α Eri	37 N	313 W
T53	2009-04-19	α Eri	39 N	296 W
T56	2009-06-06	η UMa	43 S	80 W
T58	2009-07-08	η UMa	11 S	31 W

4.3.2 Wavelength Selection

This analysis focuses on a small part of the far ultraviolet (FUV) between 1850 - 1900 Å, where the dominant source of absorption is due to aerosols alone. To avoid issues with pointing drift, we consider all wavelengths in this band as a single wavelength bin, which also improves simple photon counting statistics. Chemical models do predict the possible existence of C₆N₂, which also absorbs in this region. As discussed in Koskinen et al. (2011), it may be responsible for some absorption at altitudes above the detached haze layer, and therefore the profiles derived here may be essentially considered upper limits on the contribution from aerosol particles in the region above 700 km.

4.4 UVIS Data Acquisition and Reduction Methodology

Details on the UVIS instrument and initial data processing is contained in Esposito et al. (2004) and online in the *Cassini* UVIS Users Guide (2012) available in the NASA PDS. After this initial processing, reduction of the raw UVIS data proceeds in a relatively straightforward fashion. We combine photon counting statistics for the selected wavelength region (1850 - 1900 Å) with output from *Cassini* onboard geometer to obtain a profile of observed photon counts with occultation ray height. The occultation ray height is defined as the tangent height of the light rays as they pass from the stellar source, through Titan’s atmosphere, to the UVIS instrument onboard *Cassini*. Significant features, including extinction from the detached haze layer, are already apparent in the observed profiles even at this basic level of processing. In Figures 4.1, 4.2, 4.3, and 4.4, the left panels show the measured transmission for each Titan flyby. This measured transmission is given by Equation 4.1:

$$T = \frac{I(h)}{I_0} \quad (4.1)$$

In Equation 4.1, $I(h)$ is the measured intensity at ray height h , and I_0 is the measured intensity

from the unattenuated stellar source above the atmosphere. The uncertainty associated with this value is taken as the combination of the scatter in each ray height bin (adopted here as 20 km), as well as the standard deviation of the measured I_0 value from all records above a ray height of 1200 km. The resulting 1- σ uncertainty in transmission is encapsulated as error bars in Figures 4.1 - 4.4. The equivalent plots in line of sight optical depth are shown in the middle panels. Line of sight optical depth is defined by Equation 4.2:

$$\tau(h) = -\ln\left(\frac{I(h)}{I_0}\right) \quad (4.2)$$

The line of sight optical depths are the fundamental constraints on any forward model of atmospheric absorption, but using a basic assumption of a spherically symmetric atmosphere along the line of sight, the line of sight optical depths can be converted into the local aerosol properties as a function of altitude. Without *a priori* knowledge of the aerosol size distribution or number densities, the attenuation coefficient, α (km^{-1}), is the physical parameter that describes the degenerate effect of these two properties. This parameter is related to the line of sight optical depth through the inverse Abel transform, shown in Equation 4.3:

$$\alpha(r) = -\frac{1}{\pi} \int_r^\infty \frac{d\tau(h)}{dh} \frac{dh}{\sqrt{h^2 - r^2}} \quad (4.3)$$

In this case, r is the altitude and h is the ray height defined relative to Titan's center. The uncertainties for optical depth are propagated through this formula, and result in the 1- σ error bars reported in the right panels of Figures 4.1 - 4.4.

4.5 Discussion

There appears to be a distinct correlation in features between Titan flybys of similar season and latitude. The strongest similarities appear to be tied by season, as the four figures each contain fairly consistent snapshots of the state of Titan's haze layers over the course of a few months. The profile from T47-II is a distinct outlier, however. No detached haze layer appears present at all, and there is a monotonic increase in attenuation coefficient with a decrease in altitude. This is highly unusual, and may be correlated with the high northern latitude of this observation. It is interesting to note, however, that T40 probes a similarly high latitude, but still shows an obvious haze layer at around 500 km.

Depending on flyby, the constraints on the vertical profiles of attenuation coefficient vary from about 20% to a factor of 5 or more. This is most apparent in the region above 700 km, and in most cases these values should be considered upper limits, both due to limited sensitivity as well as the possible effects of absorption from C_6N_2 mentioned earlier in this work. Another reason

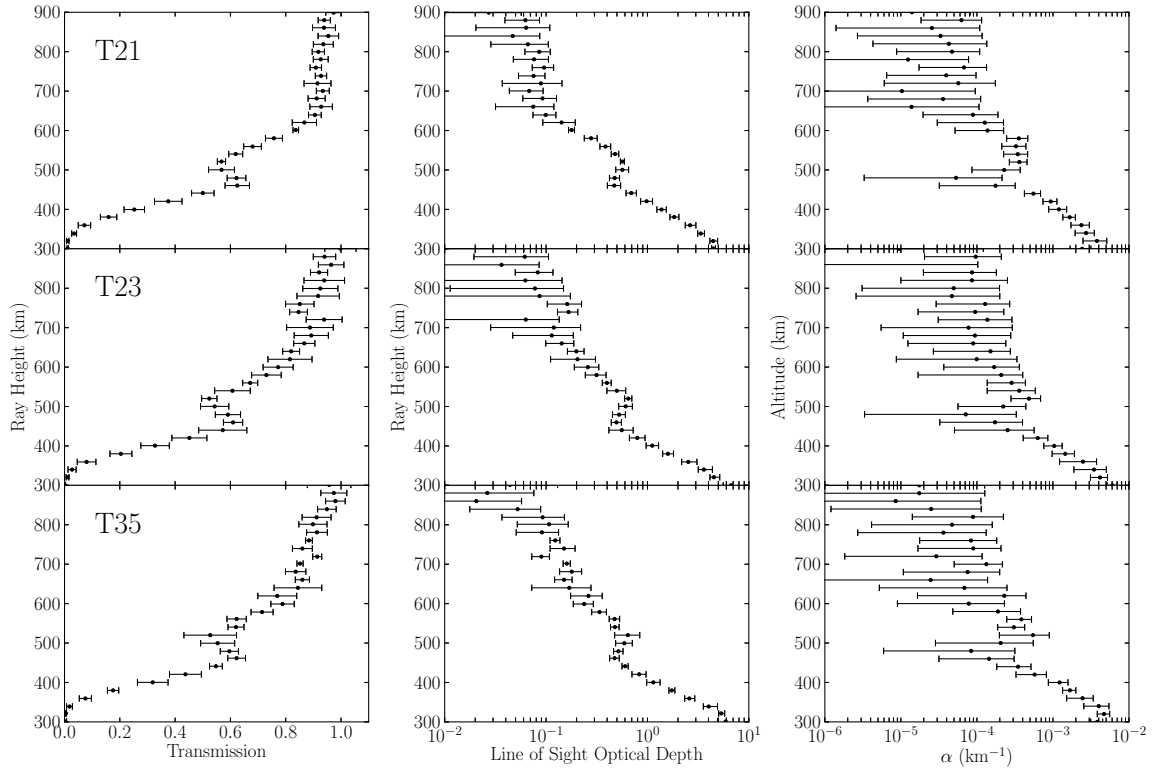


Figure 4.1 Panels showing the UVIS datasets at several stages of processing. Left: The observed transmission of the wavelengths between 1850 - 1900 Å for each flyby, with associated 1- σ uncertainties. Middle: The equivalent profiles of line of sight optical depth for each flyby, with propagated uncertainties. Right: The derived values for attenuation coefficient α with units of km^{-1} . These derived profiles assume a spherically symmetric atmosphere.

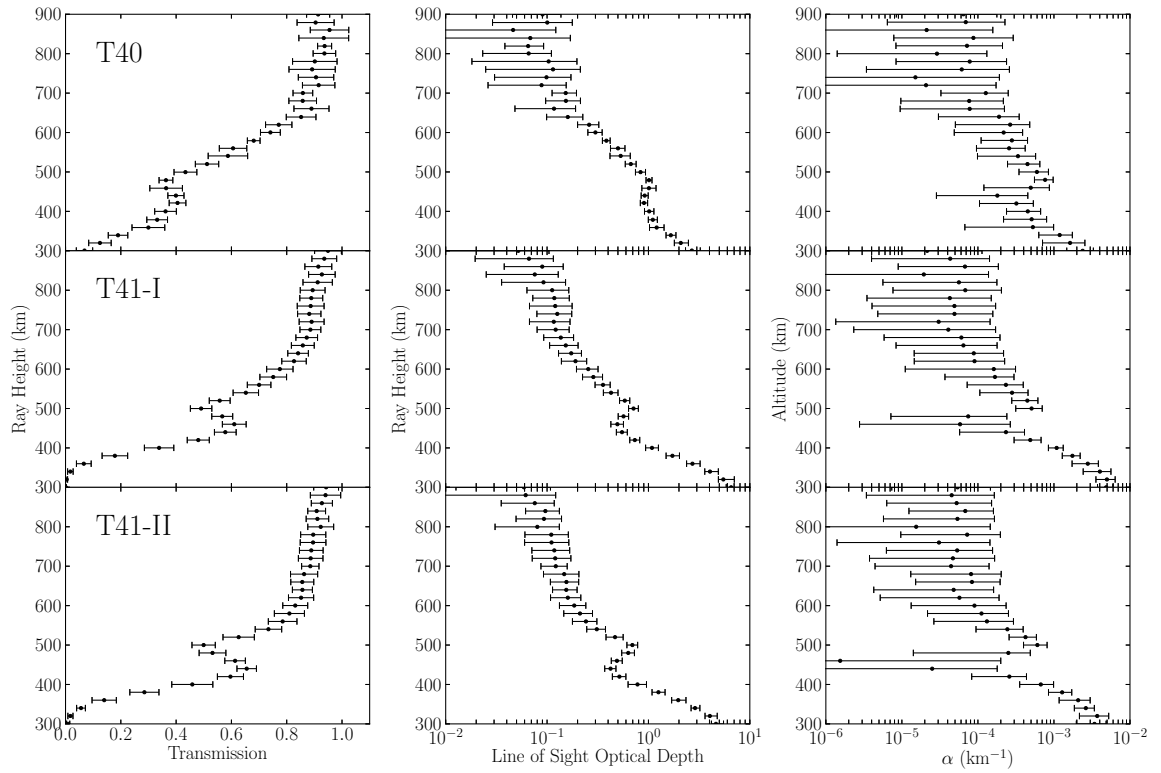


Figure 4.2 Panels showing the UVIS datasets at several stages of processing. Left: The observed transmission of the wavelengths between 1850 - 1900 Å for each flyby, with associated 1- σ uncertainties. Middle: The equivalent profiles of line of sight optical depth for each flyby, with propagated uncertainties. Right: The derived values for attenuation coefficient α with units of km^{-1} . These derived profiles assume a spherically symmetric atmosphere.

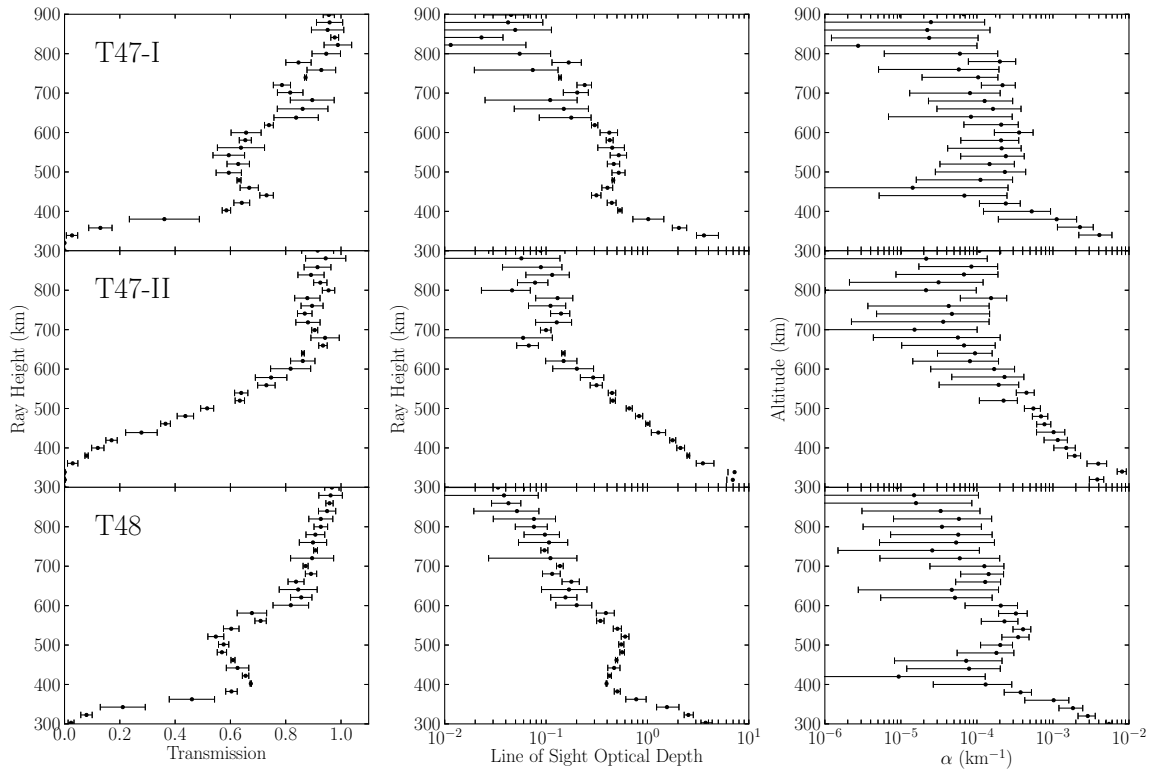


Figure 4.3 Panels showing the UVIS datasets at several stages of processing. Left: The observed transmission of the wavelengths between 1850 - 1900 Å for each flyby, with associated 1- σ uncertainties. Middle: The equivalent profiles of line of sight optical depth for each flyby, with propagated uncertainties. Right: The derived values for attenuation coefficient α with units of km^{-1} . These derived profiles assume a spherically symmetric atmosphere.

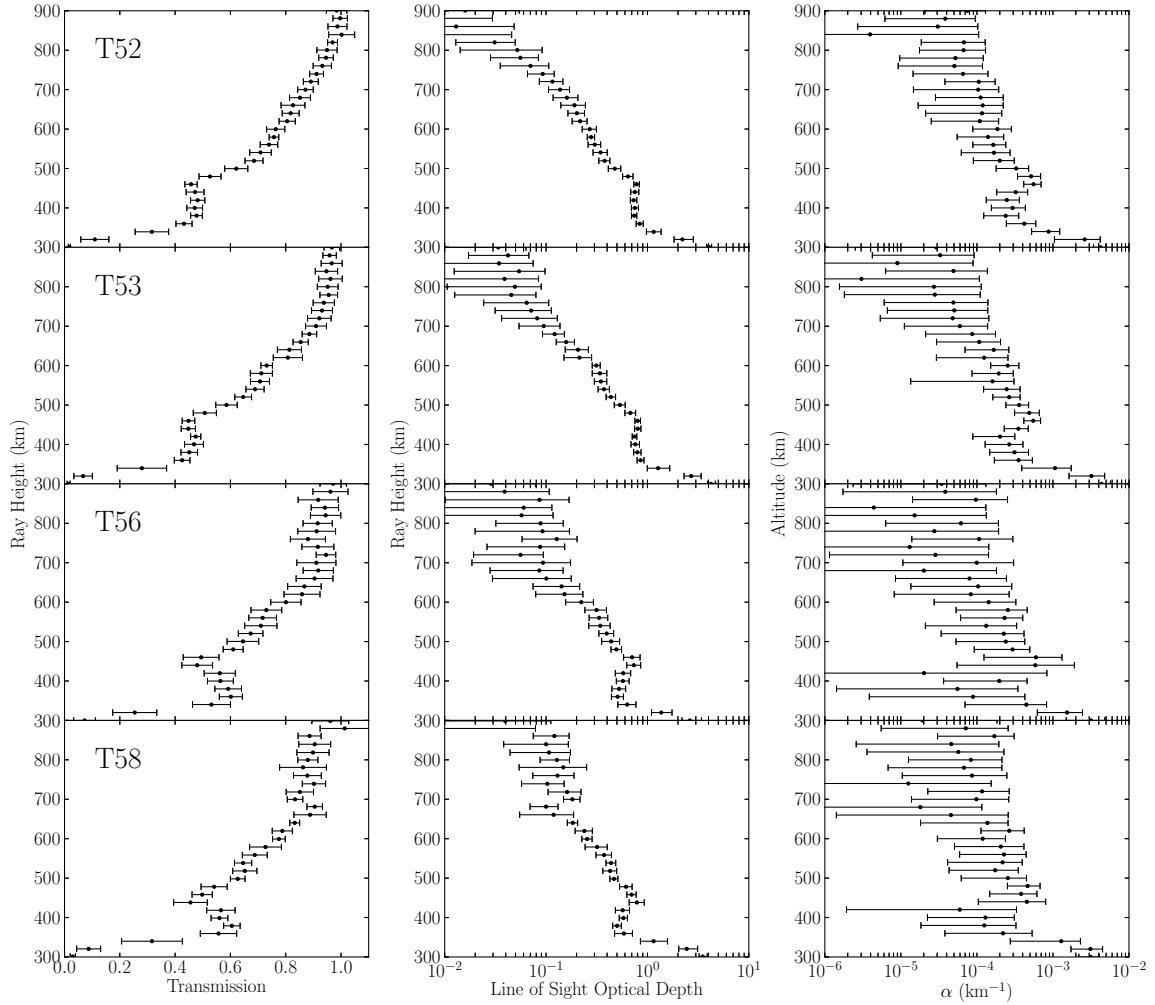


Figure 4.4 Panels showing the UVIS datasets at several stages of processing. Left: The observed transmission of the wavelengths between 1850 - 1900 Å for each flyby, with associated 1- σ uncertainties. Middle: The equivalent profiles of line of sight optical depth for each flyby, with propagated uncertainties. Right: The derived values for attenuation coefficient α with units of km^{-1} . These derived profiles assume a spherically symmetric atmosphere.

for the relatively large uncertainties is the degree of correlation between altitude layers. Inversion through the Abel transform assumes spherical symmetry, and while this assumption may be a good approximation, a more robust retrieval might include a model for latitude-dependent aerosol layer heights and properties.

In order to obtain consistent photon counting statistics for all observations, the vertical height bins are 20 km in all cases. This approach inherently filters smaller scale fluctuations, however, and for some flybys (most notably T41 and T53) smaller bins may be used. Results are not significantly different from those shown here, but more strongly suggest the complete dropout in attenuation coefficient for the altitude range around 450 km for T41 and 400 km for T53. Further modeling may be needed to fully capture this omnipresent feature.

4.6 Conclusions

The 13 FUV stellar occultations analyzed in this work provide an intriguing look at how Titan's haze layers are distributed in space and time. If additional UVIS observations can be added to this existing data set, it would allow for even better temporal coverage of the changing seasons on Titan, and also reveal what part latitude and longitude play in determining the vertical profiles of aerosol properties. The current orbital orientation of *Cassini* may preclude many further opportunities to observe occultations of UV-bright stars, but perhaps there will still be favorable geometry before the end of the *Cassini* mission in 2017.

The data sets in this work and those of previous upper atmospheric studies using UVIS (Koskinen et al., 2011; Capalbo et al., 2013; Kammer et al., 2013), as well as studies using other instruments onboard *Cassini*, provide invaluable constraints for models of Titan tholin formation and transport. Although it still remains difficult to disentangle the combined effects of aerosol number density and absorption properties, further work analyzing aerosol scattering may yield some leverage on this problem. In any case, the three-pronged approach of laboratory work, computational modeling, and observations made at Titan will yield further insights into how Titan aerosols form, chemically evolve, and are transported through the upper atmosphere.

4.7 Acknowledgements

This research was supported in part by the *Cassini* UVIS program via NASA grant JPL.1459109 to the California Institute of Technology. YLY was supported in part by NASA grant NNX09AB72G to the California Institute of Technology. DES was supported through Space Environment Technologies.

Bibliography

- Cable, M. L., et al. 2012, *Chemical Reviews*, 112, 1882
- Capalbo, F. J., et al. 2013, *The Astrophysical Journal Letters*, 766, L16
- Dutuit, O., et al. 2013, *The Astrophysical Journal Supplemental Series*, 204, 20
- Esposito, L., et al. 2004, *The Cassini-Huygens Mission*, 299
- Hörst, S. M., and Tolbert, M. A. 2013, *The Astrophysical Journal Letters*, 770, L10
- Kammer, J. A., et al. 2013, *Planetary Space Science*, 88, 86
- Khare, B. N., et al. 1984, *Icarus*, 60, 127
- Koskinen, T., et al. 2011, *Icarus*, 216, 507
- Krasnopolsky, V. A. 2009, *Icarus*, 201, 226
- Lavvas, P. P., et al. 2008a, *Planetary and Space Science*, 56, 27
- Lavvas, P. P., et al. 2008b, *Planetary and Space Science*, 56, 67
- Lavvas, P. P., et al. 2009, *Icarus*, 201, 626
- Lavvas, P. P., et al. 2010, *Icarus*, 210, 832
- Lavvas, P. P., et al. 2011a, *The Astrophysical Journal*, 728, 80
- Lavvas, P. P., et al. 2011b, *Icarus*, 213, 233
- Lavvas, P. P., et al. 2013, *Proceedings of the National Academy of Sciences*, 110, 2729
- Liang, M., et al. 2007, *The Astrophysical Journal Letters*, 661, L199
- Mandt, K. E., et al. 2012, *The Astrophysical Journal*, 749, 160
- NASA-PDS 2012, *Cassini UVIS User's Guide*,
Planetary Data System - <http://pds-rings.seti.org/cassini/uvis/index.html>

- Shemansky, D. E., et al. 2005, *Science*, 308, 978
- Thissen, R., et al. 2009, *Journal of Physical Chemistry A*, 113, 11211
- Vuitton, V., et al. 2007, *Icarus*, 191, 722
- Vuitton, V., et al. 2008, *Journal of Geophysical Research-Planets*, 113, E05007
- Vuitton, V., et al. 2009, *Planetary Space Science*, 57, 1558
- West, R. A., et al. 2011, *Geophysical Research Letters*, 38, L06204
- Yoon, Y. H., et al. 2014, *Icarus*, 233, 233

Chapter 5

A Spitzer Search for Transits of Radial Velocity Detected Super-Earths

Originally published as:

Kammer, J. A., et al. 2014, *The Astrophysical Journal*, 781, 103

5.1 Summary

Unlike hot Jupiters or other gas giants, super-Earths are expected to have a wide variety of compositions, ranging from terrestrial bodies like our own to more gaseous planets like Neptune. Observations of transiting systems, which allow us to directly measure planet masses and radii and constrain atmospheric properties, are key to understanding the compositional diversity of the planets in this mass range. Although Kepler has discovered hundreds of transiting super-Earth candidates over the past four years, the majority of these planets orbit stars that are too far away and too faint to allow for detailed atmospheric characterization and reliable mass estimates. Ground-based transit surveys focus on much brighter stars, but most lack the sensitivity to detect planets in this size range. One way to get around the difficulty of finding these smaller planets in transit is to start by choosing targets that are already known to host super-Earth sized bodies detected using the radial velocity technique. Here we present results from a *Spitzer* program to observe six of the most favorable RV-detected super-Earth systems, including HD 1461, HD 7924, HD 156668, HIP 57274, and GJ 876. We find no evidence for transits in any of their $4.5 \mu\text{m}$ flux light curves, and place limits on the allowed transit depths and corresponding planet radii that rule out even the most dense and iron-rich compositions for these objects. We also observed HD 97658, but the observation window was based on a possible ground-based transit detection (Henry et al., 2011) that was later ruled out; thus the window did not include the predicted time for the transit detection recently made by

MOST (Dragomir et al., 2013).

5.2 Introduction

Super-Earths are a unique class of planets that have masses ranging between that of Earth and Neptune. They may form via diverse pathways (e.g., Hansen & Murray, 2012; Chiang & Laughlin, 2013), and current observational constraints indicate a wide range of bulk densities and compositions for these planets (Valencia et al., 2010, 2013; Fortney et al., 2013). By characterizing the properties of these unique worlds, which have no solar system analogue, we can learn more about their physical properties and their corresponding formation channels. Although results from the Kepler survey indicate that super-Earths are common (Howard et al., 2012; Fressin et al., 2013), current surveys have found only three super-Earths (GJ 1214 b, 55 Cnc e, HD 97658 b) in transit around stars bright enough to enable these planets' detailed atmospheric characterization. This kind of characterization is crucial for constraining the bulk compositions of these planets, as the presence of a thick atmosphere leads to degeneracies in models of their interior structure (e.g., Rogers & Seager, 2010).

Methods for finding nearby transiting super-Earths include efforts from both the ground and space. Ground-based transit surveys typically focus on observations of smaller M-type stars (Berta et al., 2012; Jacobbe et al., 2012; Kovács et al., 2013), as these have more favorable planet-star radius ratios; however, to date these ground-based surveys have yielded only one super-Earth discovery, that of GJ 1214 b (Charbonneau et al., 2009), and their sensitivity to transits around larger Sun-like stars is limited. Space telescopes offer several advantages over ground-based transit surveys, as they are typically more sensitive and can observe their targets continuously. In 2017, the *TESS* space telescope will begin an all-sky survey of bright, nearby FGKM dwarf stars (Ricker et al., 2010). Until that time, searches for transits of super-Earths detected using the radial velocity method provide a promising route to increase the number of such systems. This approach has resulted in the discovery of transits for 55 Cnc e and HD 97658 b (Winn et al., 2011; Dragomir et al., 2013) by the *MOST* space telescope.

The *Spitzer* space telescope provides a comparable platform for transit surveys of RV-detected super-Earths, and benefits from a higher photometric precision than *MOST*. Gillon et al. (2010, 2012) have previously utilized *Spitzer* to rule out transits for the super-Earth HD 40307 b and to further characterize the properties of the transiting super-Earth 55 Cnc e as part of a search for nearby transiting low-mass planets. This paper presents the results of six additional *Spitzer* observations of super-Earth systems. In §5.3 we overview the radial velocity data and transit window predictions for these objects. We provide descriptions of the 4.5 μm *Spitzer* observations along with data reduction methods and transit model analysis in §5.4, followed by discussion and conclusions of this work in

§5.5 and §5.6, respectively.

5.3 Target System Properties and Radial Velocity Measurements

5.3.1 System Properties

HD 1461 b has a minimum mass of $8.1M_{\oplus}$ and orbits a G-type star with a period of 5.77 days. Its eccentricity is estimated to be fairly low at 0.16. Two other planets with minimum masses of 28 and $87M_{\oplus}$ may exist in the system at periods of 446 and 5017 days but have yet to be confirmed (Rivera et al., 2010a).

HD 7924 b has a minimum mass of $9.26M_{\oplus}$ and orbits a K-type star with a period of 5.40 days. Eccentricity of the planet is close to zero and fixed at this value in the fits here. No additional planets have been reported in this system (Howard et al., 2009).

HD 97658 b has a minimum mass of $8.2M_{\oplus}$ and orbits a K-type star with a period of 9.50 days. Its eccentricity is estimated at around 0.13. No other planets have been reported in this system (Howard et al., 2011b). Note that a transit detection and further constraints on planet properties have been recently made by Dragomir et al. (2013) using *MOST*; see §4 for details and discussion of this target.

HD 156668 b has a minimum mass of $4.15M_{\oplus}$ and orbits a K-type star with a period of 4.64 days. Orbital solutions from fits to RV measurements were found for both eccentricities of 0 (fixed) and 0.22, and include the possible effects of one additional planet candidate in the system with a minimum mass of $45M_{\oplus}$ and a period of 810 days (Howard et al., 2011a).

HIP 57274 b has a minimum mass of $11.6M_{\oplus}$ and orbits a K-type star with a period of 8.14 days. Orbital solutions from fits to RV measurements were found for both eccentricities of 0 (fixed) and 0.20. HIP 57274 also has two additional detected planets in the system, one with a minimum mass of $0.4M_{Jup}$ and a period of 32 days, and the other with a minimum mass of $0.53M_{Jup}$ and a period of 432 days (Fischer et al., 2012).

GJ 876 d has a minimum mass of $5.85M_{\oplus}$ and orbits an M-type star with a period of 1.94 days. This planet is estimated to have an eccentricity of about 0.21, and is the inner-most planet in a system with at least three others. These include a second planet with a minimum mass of $0.71M_{Jup}$ and a period of 30 days, and a third planet with a minimum mass of $2.3M_{Jup}$ and a period of 61 days (Rivera et al., 2005; Correia et al., 2010). A fourth planet was also recently detected with a minimum mass of $14.6M_{\oplus}$ and a period of 124 days (Rivera et al., 2010b).

Table 5.1. Target System Properties

Target	Stellar Type ^a	$R_*(R_\odot)$ ^a	$M \sin i (M_\oplus)$	Period (days)	e	Calculated T_0 ^b
HD 1461 b	G3 V	1.2441 ± 0.0305	8.1 ± 0.7	5.77267 ± 0.00029	0.16 ± 0.05	5089.041 ± 0.090
HD 7924 b	K0 V	0.7821 ± 0.0258	9.26 ± 1.77	5.39699 ± 0.00013	0 (fixed)	5089.757 ± 0.037
HD 97658 b	K1 V	0.68 ± 0.02	8.2 ± 1.2	9.4957 ± 0.0022	0.13 ± 0.07	5650.681 ± 0.012
HD 156668 b	K3 V	0.720 ± 0.013	4.15 ± 0.58	4.64230 ± 0.00070	0 (fixed)	5855.86 ± 0.12
				4.64260 ± 0.00078	0.22 ± 0.08	5856.18 ± 0.23
HIP 57274 b	K5 V	0.68 ± 0.03	11.6 ± 1.3	8.1391 ± 0.0051	0 (fixed)	5932.31 ± 0.27
				8.1389 ± 0.0049	0.20 ± 0.10	5932.25 ± 0.32
GJ 876 d	M4 V	0.3761 ± 0.0059	5.85 ± 0.39	1.93778 ± 0.00002	0.207 ± 0.055	6159.09 ± 0.16^c

^aStellar properties for HD 1461, HD 7924, and GJ 876 cited from von Braun et al. (2013); other stellar properties cited from RV discovery papers.

^bJD - 2,450,000

^cCalculated from an N-body simulation that accounts for perturbations from other planets in the system.

5.3.2 Radial Velocity Ephemerides

The required length of the observation window, and therefore the constraint that radial velocity measurements placed on ephemerides, limited the initial selection of targets for transit investigation. We chose six targets for this *Spitzer* program that had relatively low uncertainties for their predicted transit times and for most cases required observation windows with durations less than 20 hours. We also excluded any super-Earths with existing *Spitzer* observations spanning predicted transit windows.

Details on the target system properties and the RV determined ephemerides are given in Table 5.1. We utilize updated ephemerides obtained by a fit to both published and unpublished data for these systems from the California Planet Search group (Howard et al., in prep). Our fits for HD 1461 b appear to prefer an eccentric solution, and we therefore leave eccentricity as a free parameter. For HD 7924 b we assume a circular orbit for the planet, as there was no convincing evidence for a non-zero eccentricity. We used the preliminary transit detection from Henry et al. (2011) to define our transit window for HD 97658 b; see §4 for a complete discussion of this target. For HD 156668 b and HIP 57274 b there was marginal evidence for non-zero eccentricities, and we therefore selected modestly longer transit windows spanning both the circular and eccentric predictions for the transit time. The transit times of GJ 876 d are expected to deviate from a linear ephemeris due to perturbations from the other planets in the system, and we therefore calculated individual transit windows spanning the epoch of our observations using an N-body integration of the planet parameters given in Table 2 of Rivera et al. (2010b).

Table 5.2. *Spitzer* Observation Details

Target	UT Start Date	AOR	Duration (hrs)	n_{img}^a	t_{int} (s) ^b	r_{apr}^c	Start - End ^d	Predicted T_c ^d
HD 1461 b	2011-08-31	42790656	12.9	355,008	0.1	2.46	5804.52 - 5805.06	5804.85 ± 0.10
HD 7924 b	2011-11-01	44605184	7.9	217,600	0.1	2.37	5866.74 - 5867.07	5866.92 ± 0.04
HD 97658 b	2012-02-25	42608128	11.9	327,616	0.1	2.35	5982.73 - 5983.22	5983.03 ± 0.08
HD 156668 b ^e	2012-05-03	42790912	17.3	145,856	0.4	2.86	6050.65 - 6051.37	6050.84 ± 0.12 6051.17 ± 0.23
HIP 57274 b ^e	2012-03-02	44273920	15.9	134,080	0.4	2.58	5988.93 - 5989.59	5989.28 ± 0.27 5989.22 ± 0.32
GJ 876 d	2012-08-19	42791424	12.4	338,560	0.1	2.63	6158.79 - 6159.29	6159.09 ± 0.16

^aTotal number of images.

^bImage integration time.

^cMedian aperture radius (pixel widths) from noise pixel flux calculation.

^dJD - 2,450,000

^eAs in Table 5.1, predicted T_c are shown for both zero (first row) and non-zero (second row) eccentricity fits.

Table 5.3. Limits on Transit Probability

Target	$M \sin i$ (M_{\oplus})	2σ limits (R_{\oplus}) ^a	Model radii (R_{\oplus}) ^b	a priori ^{c,d}	a posteriori ^e
HD 1461 b	8.1 ± 0.7	0.64 – 1.02	1.34, 1.86, 2.46	9.1%	0.15%
HD 7924 b	9.26 ± 1.77	0.96 – 1.16	1.38, 1.93, 2.54	6.4%	0.0016%
HD 97658 b ^f	8.2 ± 1.2	0.90 – 1.00	1.34, 1.87, 2.47	3.8%	0.029%
HD 156668 b ^g	4.15 ± 0.58	0.82 – 0.88	1.13, 1.56, 2.07	6.7%	0.44%
					1.4%
HIP 57274 b ^g	11.6 ± 1.3	0.72 – 0.82	1.45, 2.03, 2.69	4.5%	1.0%
					1.4%
GJ 876 d	5.85 ± 0.39	0.52 – 0.70	1.23, 1.71, 2.27	8.3%	1.1%

^aCalculated limits on planetary radius derived from fits to light curves using impact parameters of 0 to 0.95.

^bModel radii derived from the minimum mass found by RV measurements, calculated for planet compositions corresponding to 100% Fe, 100% MgSiO₃, and 100% H₂O (Zeng & Sasselov, 2013).

^cTransit probability before observations, calculated simply as the ratio of R_*/a_p . Non-zero eccentricity will also influence this value; the exact effect is not well-constrained for these targets but for an eccentricity of 0.2 it will lead to at most $\pm 0.3 - 1.0\%$ difference in transit likelihood.

^dOther factors also influence prior transit likelihood besides geometry; known exoplanet mass occurrence rates combined with minimum mass estimates from RV measurements increase transit likelihood for RV-detected super-Earths (e.g., $P_{tr} = 12.5\%$ for HD 1461 b, Stevens & Gaudi, 2013).

^eTransit probability after observations.

^fSee §5.5 for discussion of a transit detection outside the observation window (Dragomir et al., 2013).

^gPosterior transit probabilities are shown for both zero (first row) and non-zero (second row) eccentricity fits.

5.4 *Spitzer* Data Acquisition and Reduction Methodology

5.4.1 Photometry and Intrapixel Sensitivity

These observations were obtained using the Infra-Red Array Camera (IRAC) in the 4.5 μm channel operated in sub-array mode; additional details are shown in Table 5.2. There is a known instrumental effect during *Spitzer* observations that consists of a ramp up in pixel sensitivity with time, usually occurring up to an hour in duration at the start of an observation. We therefore padded our light curves with additional time before the predicted center of transit in case it was necessary to trim the initial data affected by the ramp, as is standard practice in *Spitzer* analyses. This results in a slightly off-center observation window for each of our targets with regards to their predicted centers of transit.

In all data sets, we extract flux information from the BCD files provided by the *Spitzer* pipeline. We calculate the flux using techniques described in several previous studies (Knutson et al., 2012; Lewis et al., 2013; Todorov et al., 2013). First, we find the center of the stellar point spread function using a flux-weighted centroiding routine, then we perform aperture photometry, testing both fixed and time variable aperture sizes. The fixed aperture radii we tested ranged from 2.0 to 3.0 pixel widths, in steps of 0.1; the time variable apertures were scaled based on the noise pixel parameter (Mighell, 2005). The noise pixel parameter is proportional to the square of the full width half max of the stellar point spread function, and described by Equation 5.1 below:

$$\beta = \frac{(\sum_n I_n)^2}{\sum_n I_n^2} \quad (5.1)$$

where I_n is the measured intensity of the n^{th} pixel.

We then empirically re-scale the noise pixel aperture radii either as $r = a\sqrt{\beta}$, where a is a scaling factor between 0.8 and 1.7 pixel widths, in steps of 0.1; or alternatively as $r = \sqrt{\beta} + C$, where C is a constant between -0.2 and 1.0 pixel widths, also in steps of 0.1.

We account for variations in intrapixel sensitivity by adopting a nearest neighbor weighting algorithm, such that the flux at each time step is normalized by a weighted sum of its 50 nearest neighbors in X and Y space on the pixel array, as described in Knutson et al. (2012) and Lewis et al. (2013).

We then evaluate each of the aperture radius models to find the lowest resulting scatter in the residuals of the fitted light curve. Although the best fit aperture radius varied depending on target, in each case an adjustment based on noise pixel yielded improvements over fixed aperture photometry; however, both methods resulted in null transit detections. The median best fit aperture radius for each light curve is shown in Table 5.2. Figure 5.1 shows the raw flux photometry for each observation. Figure 5.2 shows the corresponding normalized flux photometry after utilizing the nearest neighbor

algorithm.

5.4.2 Transit Models and Uncertainty Estimation

We fix the orbital parameters for each planet to the values obtained from the radial velocity measurements, and only the time of transit center, the planet radius, and the impact parameter are varied in the fits. The forward model for a transit (Mandel & Agol, 2002) takes as input these three transit parameters, as well as the orbital period and planet semi-major axis from RV measurements, and limb darkening coefficients based on each target’s stellar parameters (Sing, 2010).

Characterization of transit parameter posterior likelihoods is carried out using a pseudo-grid search method: given a fixed impact parameter and transit center time, a best fit planet radius is found by Levenberg-Marquardt chi-squared minimization. Planet radius is effectively allowed to be negative in these fits by calculating a transit light curve using the absolute value of the planet radius, then inverting the curve for negative radius values. This is done in order not to bias the fits and to better characterize the noise level of the observations. Figure 5.3 shows histograms of planetary radii for a fixed impact parameter of zero (an equatorial transit), and fixed transit center times that are stepped across the window of observation in increments of approximately 30 seconds. This effectively finds the best fit planet radius at each location in the light curve. As no significant transits are detected in any of the light curves, these histograms characterize the magnitude of the combined Gaussian (white) and time correlated (red) noise, and therefore provide empirical thresholds for detection of possible transits. 2σ limits are calculated that encompass 95% of the histogram (i.e., 47.5% of the distribution lies above the median and below the upper limit, 47.5% below the median and above the lower limit). The 2σ limits corresponding to positive planetary radii are then taken as thresholds for transit detection, as negative radii are non-physical solutions. These 2σ thresholds are shown in Table 5.3, along with values of planet radii corresponding to models with 100% Fe, 100% MgSiO₃, and 100% H₂O bulk composition (Zeng & Sasselov, 2013), derived using the planet minimum masses found from RV measurements. Although we expect that a pure iron planet would be very unlikely based on current planet formation models, this limiting case allows us to place a strict lower limit on the range of possible radii for our target planets. Our estimated radii also assume that the planets have negligible atmospheres, and the presence of a thick atmosphere would only serve to increase the transit depth for a given interior composition.

In addition to determining transit detection limits, we confirm the validity of these limits by inserting artificial transits with depths above the detection threshold into the data and verifying that we can reliably retrieve them in our fits. Analysis of these artificially inserted transits yielded consistent results for detection thresholds of planetary radii.

In Figure 5.4 we evaluate the sensitivity of our detection limits to changes in the assumed impact parameter b . We find that our limits on planetary radius are fairly insensitive to changes in impact

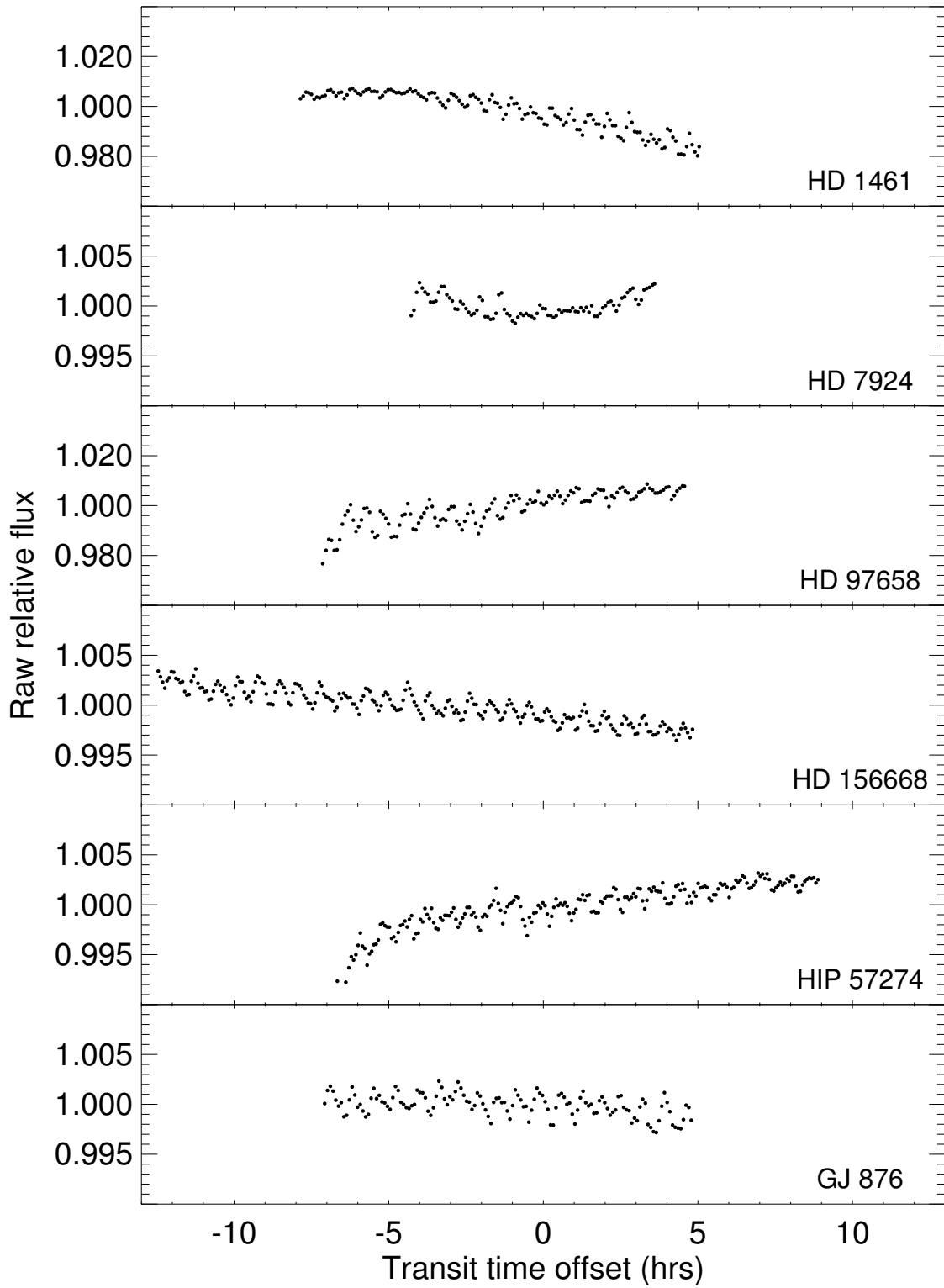


Figure 5.1 Raw *Spitzer* 4.5 μm light curves. Relative flux is shown binned at 5 minute intervals. Intrapixel sensitivity variations cause distinct sawtooth patterns as a result of the X and Y center position of the stellar point spread function oscillating over time.

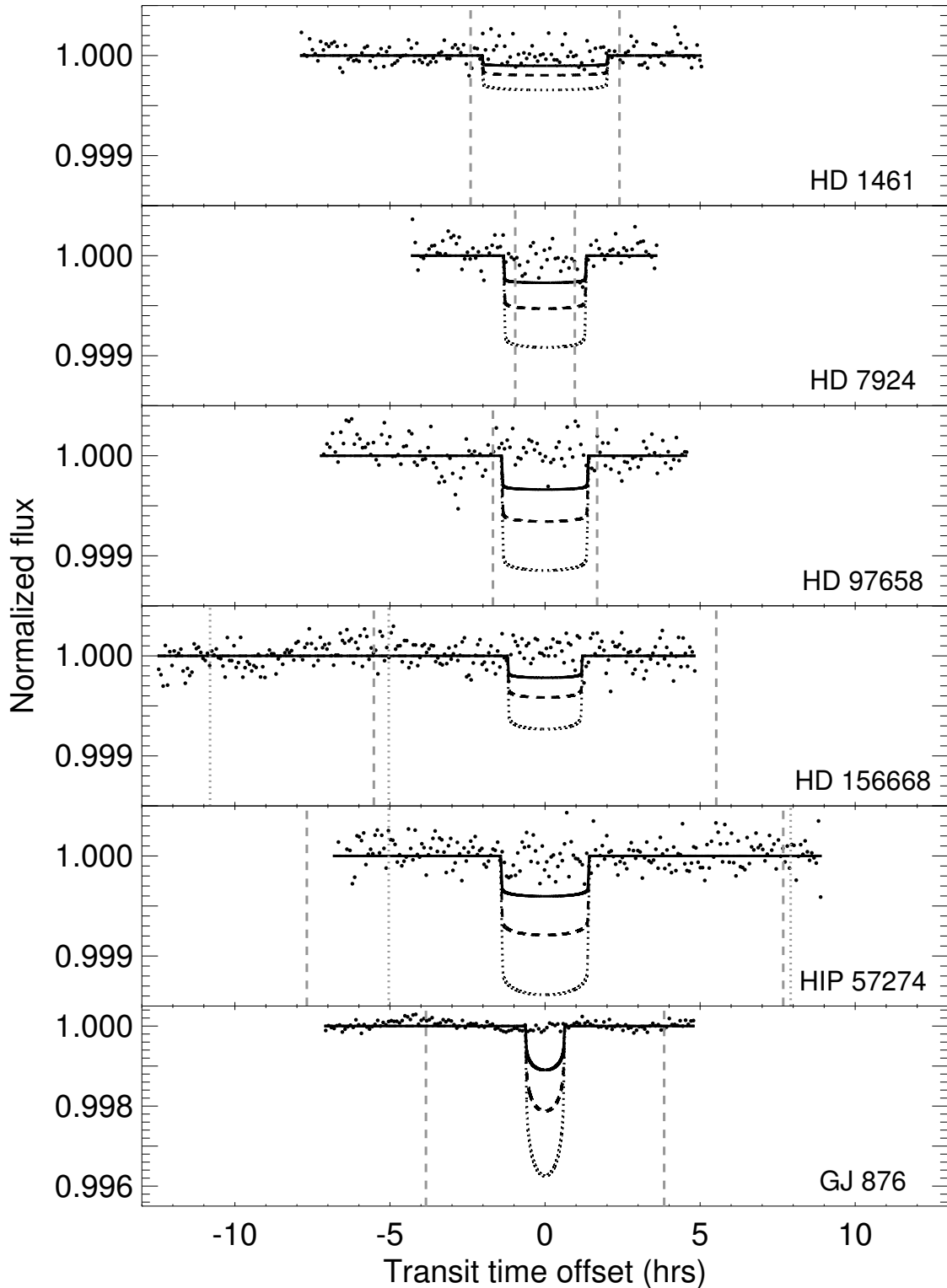


Figure 5.2 Normalized *Spitzer* 4.5 μm light curves with instrumental effects removed. The normalized flux is shown binned at 5 minute intervals, and transit model light curves for planet radii corresponding to 100% Fe (black, solid line), 100% MgSiO₃ (black, dashed line), and 100% H₂O (black, dotted line) cases are also shown for comparison. The 1 σ uncertainties for time of transit center during each light curve are marked as dashed gray vertical lines; for targets HD 156668 b and HIP 57274 b, both uncertainty regions for circular (gray, dotted) and eccentric (gray, dashed) orbital fits are plotted.

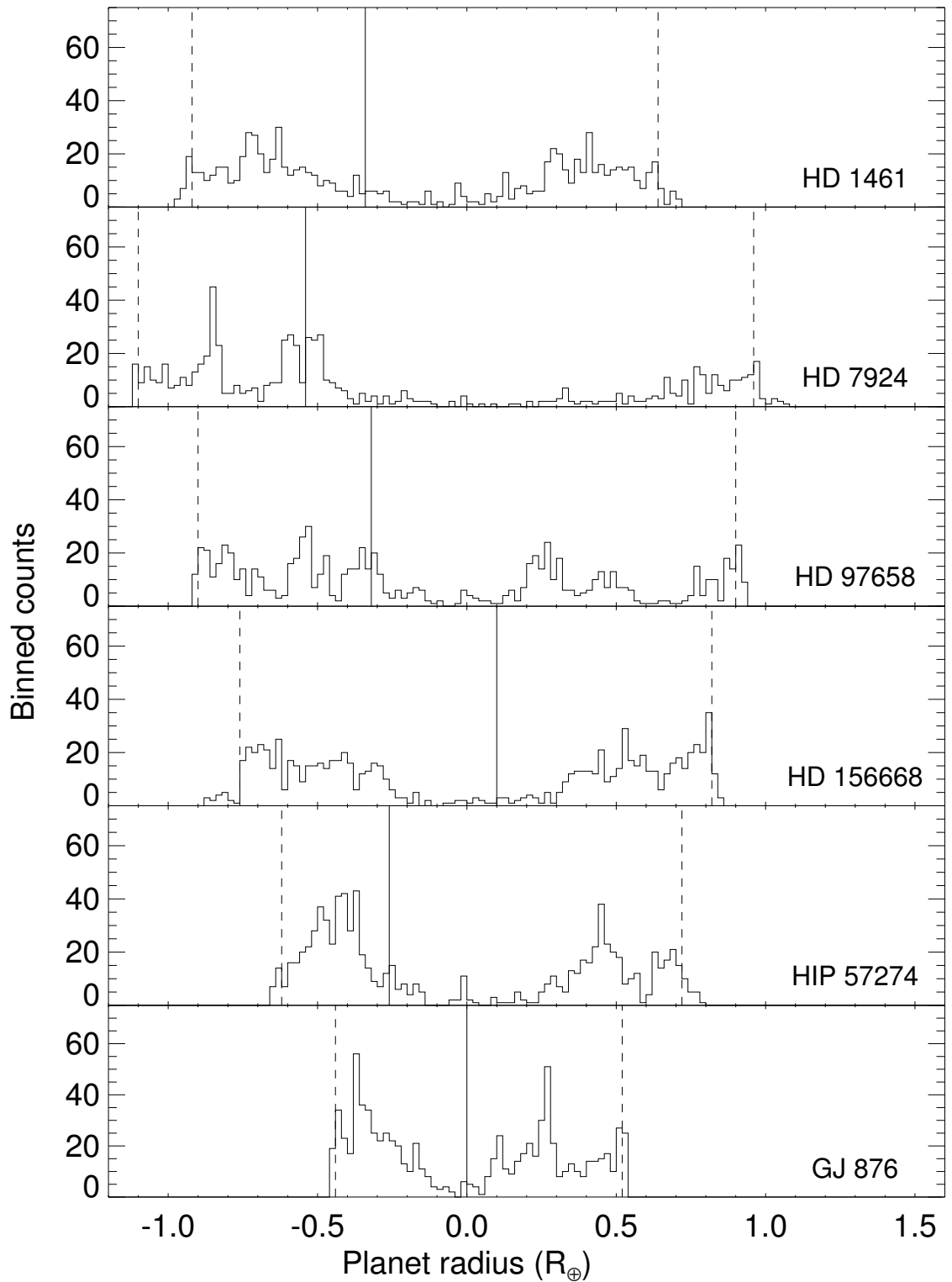


Figure 5.3 Histograms of best fit planetary radius values for a fixed impact parameter of 0. The median best fit radius is given by the solid line, and the 2σ uncertainties are given by the dashed lines; these lines may be asymmetric about the median but encompass the 95% confidence interval. These values characterize the effective noise level of the light curves.

parameter, though this sensitivity varies depending on the target. The limits for HD 97658 and HD 156668 remain nearly constant out to impact parameters of 0.9, while the thresholds for the other targets tend to vary more noticeably but still mostly remain below a planet radius of $1R_{\oplus}$. The unusual behavior of HD 7924 in this case is likely due to a correlated noise feature in the observed light curve of similar duration and depth as a model transit with an impact parameter of around 0.5 and a planet radius of about $1.1R_{\oplus}$. The relatively short duration of the HD 7924 light curve influences the sensitivity of this impact parameter test to the noise in the data, but note that even in this case, a planet radius of $1.1R_{\oplus}$ remains an unphysical solution.

5.5 Discussion

As the 2σ thresholds for possible transits are in all cases less than the radius of a pure iron core model (Zeng & Sasselov, 2013), we therefore conclude that transits for all of our targets are conclusively ruled out within the window of our observations. Table 5.3 shows the posterior likelihood that the planets may still transit outside the *Spitzer* observation windows. For several cases the probability of transit has been all but eliminated, while for others we calculate the individual probability of transit remains no higher than 1.4%.

For the case of GJ 876 d, a null transit result is in agreement with the initial photometric measurements of Rivera et al. (2005). However, we note that our non-detection of a transit for HD 97658 b appears on initial inspection to conflict with a recent paper by Dragomir et al. (2013) announcing the detection of transits with *MOST*. We centered our *Spitzer* transit window using the predicted transit time from the preliminary ground-based transit detection of Henry et al. (2011). Subsequent follow-up observations by Dragomir et al. (2012) taken within a month of our *Spitzer* observations demonstrated that the planet did not transit at the time predicted by Henry et al.; our data provide additional support for this conclusion. A later re-analysis by Henry et al. indicated that the apparent transit detection was caused by an airmass effect in the original observations.

Using the updated transit ephemeris from the recent *MOST* detection, we calculate a predicted transit center time of 2455982.17 ± 0.06 , approximately 13 hours earlier than the *Spitzer* observation window that started at 2455982.73. We therefore conclude that our non-detection of a transit for HD 97658 b is consistent with the transit ephemeris reported by Dragomir et al. (2013).

5.6 Conclusions

We find no evidence for transits in any of the systems targeted by this survey. There remains some probability that a transit occurred outside the observation window for each target; we know this occurred for HD 97658 b, but the probability is extremely small for our other targets, as shown in

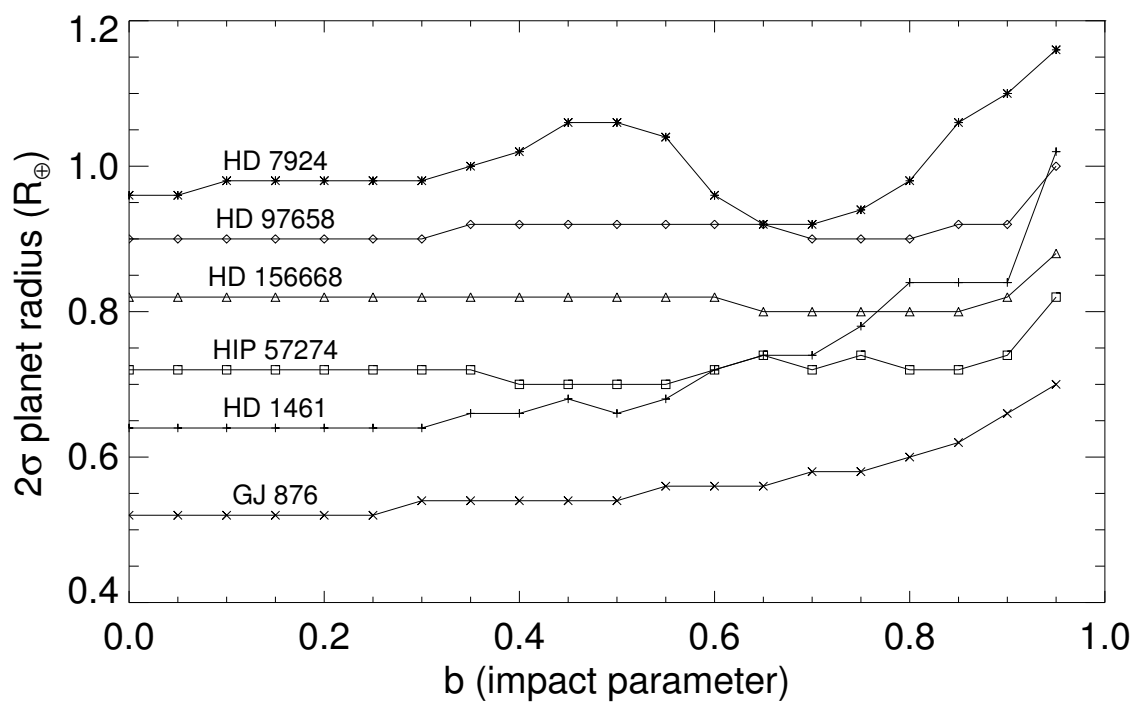


Figure 5.4 Change in detection threshold as a function of fixed impact parameter. For each target, planet radius detection limits are calculated using impact parameters ranging from 0.0 (an equatorial transit) to 0.95 (a grazing transit).

Table 5.3. Excluding HD 97658 b, we estimate that the cumulative posterior transit probability for these targets is now only 4.0%. Their cumulative prior transit probability before observations was 30.5%; it is therefore not surprising that no transits were detected, but the high value of such transiting systems more than justifies the investment of *Spitzer* time.

Although no transits were detected in this work, future prospects of utilizing this method for super-Earth discovery remain high. By our estimates the majority of stars known to host super-Earths with well-constrained ephemerides have already been observed by either *Spitzer*, *MOST*, or both, but we expect that current and next-generation radial velocity surveys will produce an ever-growing number of such systems in the coming years. Until the launch of *TESS*, this method remains one of the most promising avenues for detecting transiting super-Earths around bright, nearby stars.

5.7 Acknowledgements

J.-M.D. and N.K.L. acknowledge funding from NASA through the Sagan Exoplanet Fellowship program administered by the NASA Exoplanet Science Institute (NExSci). This work is based on observations made with the *Spitzer Space Telescope*, which is operated by the Jet Propulsion Laboratory, California Institute of Technology, under contract with NASA.

Bibliography

- Berta, Z. K., et al. 2012, *The Astronomical Journal*, 144, 145
- Charbonneau, D., et al. 2009, *Nature*, 462, 891
- Chiang, E., & Laughlin, G. 2013, *Monthly Notices of the Royal Astronomical Society*, 431, 3444
- Correia, A., et al. 2010, *Astronomy and Astrophysics*, 511, A21
- Dragomir, D., et al. 2012, *The Astrophysical Journal Letters*, 759, L41
- Dragomir, D., et al. 2013, *The Astrophysical Journal Letters*, 772, L2
- Fischer, D. A., et al. 2012, *The Astrophysical Journal*, 745, 21
- Fortney, J. J., et al. 2013, *The Astrophysical Journal*, 775, 80
- Fressin, F., et al. 2013, *The Astrophysical Journal*, 766, 81
- Giacobbe, P., et al. 2012, *Monthly Notices of the Royal Astronomical Society*, 424, 3101
- Gillon, M., et al. 2010, *Astronomy and Astrophysics*, 518, A25
- Gillon, M., et al. 2012, *Astronomy and Astrophysics*, 539, A14
- Hansen, B. M., & Murray, N. 2012, *The Astrophysical Journal*, 751, 158
- Henry, G. W., et al. 2011, *The Astrophysical Journal*, withdrawn (arXiv:1109.2549)
- Howard, A. W., et al. 2009, *The Astrophysical Journal*, 696, 75
- Howard, A. W., et al. 2011a, *The Astrophysical Journal*, 726, 73
- Howard, A. W., et al. 2011b, *The Astrophysical Journal*, 730, 10
- Howard, A. W., et al. 2012, *The Astrophysical Journal Supplement*, 201, 15
- Knutson, H. A., et al. 2012, *The Astrophysical Journal*, 754, 22
- Kovács, G., et al. 2013, *Monthly Notices of the Royal Astronomical Society*, 433, 889

- Lewis, N. K., et al. 2013, *The Astrophysical Journal*, 766, 95
- Mandel, K., & Agol, E. 2002, *The Astrophysical Journal Letters*, 580, L171
- Mighell, K. J. 2005, *Monthly Notices of the Royal Astronomical Society*, 361, 861
- Ricker, G. R., et al. 2010, *Bulletin of the American Astronomical Society*, 42, 459
- Rivera, E. J., et al. 2005, *The Astrophysical Journal*, 634, 625
- Rivera, E. J., et al. 2010a, *The Astrophysical Journal*, 708, 1492
- Rivera, E. J., et al. 2010b, *The Astrophysical Journal*, 719, 890
- Rogers, L. A., & Seager, S. 2010, *The Astrophysical Journal*, 712, 974
- Sing, D. 2010, *Astronomy and Astrophysics*, 510, A21
- Stevens, D. J., & Gaudi, B. S. 2013, *Publications of the Astronomical Society of the Pacific*, 125, 933
- Todorov, K. O., et al. 2013, *The Astrophysical Journal*, 770, 102
- Valencia, D., et al. 2013, *The Astrophysical Journal*, 775, 10
- Valencia, D., et al. 2010, *Astronomy and Astrophysics*, 516, 20
- von Braun, K., et al. 2013, *Monthly Notices of the Royal Astronomical Society*, submitted (arXiv:1312.1792)
- Winn, J., et al. 2011, *The Astrophysical Journal Letters*, 737, L18
- Zeng, L., & Sasselov, D. 2013, *Publications of the Astronomical Society of the Pacific*, 125, 227

Chapter 6

Spitzer Secondary Eclipse Observations of Three New Cool Gas Giant Planets

6.1 Summary

Atmosphere studies of relatively cool ($T_{\text{eq}} < 1200$ K) gas giant planets can provide important constraints on planet formation models, as the observed CH_4/CO ratios are closely related to the hydrogen content of their atmospheres. Unfortunately, there are only a handful of planets in this temperature range with published secondary eclipse observations. In this work, we analyze *Spitzer* 3.6 and 4.5 micron secondary eclipse observations of three new cool planets: WASP-6b, WASP-39b, and HAT-P-19b. These planets have masses ranging from 0.3 – 0.5 M_{J} and predicted equilibrium temperatures ranging between 1000 – 1150 K, assuming zero albedo and uniform redistribution of heat. For WASP-6b, we find eclipse depths of $0.1114 \pm 0.0380\%$ (3.6 μm) and $0.0965 \pm 0.0351\%$ (4.5 μm). For WASP-39b, these values are $0.0603 \pm 0.0173\%$ (3.6 μm) and $0.0484 \pm 0.0211\%$ (4.5 μm), respectively. For HAT-P-19b, they are $0.0840 \pm 0.0221\%$ (3.6 μm) and $0.0452 \pm 0.0377\%$ (4.5 μm). We compare our measured eclipse depths to the predictions of a suite of atmosphere models for each planet, and find that in all cases the measured eclipse depths are consistent with solar metallicity atmospheres. We find no evidence for temperature inversions or disequilibrium chemistry in these atmospheres, and in all cases prefer models with relatively efficient recirculation of energy to the planet’s night side. We also find that the measured eclipse times for all three planets are consistent with a circular orbit.

6.2 Introduction

Secondary eclipse observations of gas giant planets provide an invaluable tool for probing the temperature and compositional state of their atmospheres by detecting light emitted from the planet itself. Studies utilizing *Spitzer* have previously observed secondary eclipses of more than fifty transiting planets (Madhusudhan et al., 2014), but the vast majority of these objects have been Jovian-mass planets with temperatures between 1500-2500 K. The atmospheres of smaller and cooler planets remain mostly uncharted territory, in part because it is extremely challenging to detect their thermal emission at the near-infrared wavelengths accessible to most telescopes. Equilibrium chemistry models predict that at around 1000 K the dominant reservoir of atmospheric carbon shifts from CO and CO₂ to CH₄, a phenomenon similar to that which occurs in the atmospheres of cool, low-mass stars (Kirkpatrick, 2005). However, these predictions of equilibrium chemistry are dependent not only on temperature but also on the underlying elemental abundances, and therefore are sensitive to changes in atmospheric metallicity, or the amount of hydrogen present from initial formation. Increased metallicity, and thus a relatively lower amount of hydrogen, will lead to a lower abundance of CH₄ and enhanced CO, even in cooler planets where equilibrium chemistry would normally predict a methane-dominated atmosphere.

The exoplanet GJ 436b is one possible example of the observable effects of enriched atmospheric metallicity. The work of Moses et al. (2013) explored the predicted equilibrium and disequilibrium chemistry of hot Neptune-sized planets, finding that the *Spitzer* secondary eclipse observations indicating a CO-rich, CH₄-poor atmosphere for GJ 436b (Stevenson et al., 2010; Line et al., 2011) could be explained by models with higher metallicity. They also predict a continuum of possible atmospheric compositions for planets in this category, ranging from Neptune-like H₂-dominated atmospheres to Venus-like CO₂-dominated atmospheres, or even more exotic planets dominated by H₂O, CO, or O₂. In order to test these predictions, however, more secondary eclipse observations of cool planets are needed. Thus far, in addition to GJ 436b, WASP-8b (Cubillos et al., 2013), HAT-P-12b (Todorov et al., 2013), and HAT-P-20b (Deming et al., 2014) are the only cool gas giants with well-characterized secondary eclipse observations.

Studies of hydrogen-dominated atmospheres in our own solar system have shown that as core mass fraction increases, so does the atmospheric metallicity. This hypothesis holds true for Uranus and Neptune, as these planets have atmospheres enriched in carbon by a factor of about 30-40 times solar abundance, while Jupiter's atmosphere is only three times the solar value. Though these planets' bulk densities are comparable to many detected exoplanets in the same size range, it remains an open question whether the metallicities of exoplanet atmospheres follow a similar trend, as models of planet formation indicate that even slightly different conditions in protoplanetary disks can result in a large diversity of final masses and compositions (Helled & Bodenheimer, 2014).

Table 6.1. Target System Properties

Target	Stellar Type	M_p (M_J)	Period (days)	T_c ^a	e	T_{eq} (K) ^b	Ref.
WASP-6b	G8	0.480 ± 0.038	$3.361006 \pm 3 \times 10^{-6}$	5446.7662 ± 0.0006	0.041 ± 0.019	1150	^c
WASP-39b	G8	0.284 ± 0.031	$4.055259 \pm 9 \times 10^{-6}$	5342.9688 ± 0.0002	0 (fixed)	1120	^d
HAT-P-19b	K	0.292 ± 0.018	$4.008778 \pm 6 \times 10^{-6}$	5091.5342 ± 0.0003	0.067 ± 0.042	1010	^e

^aMeasured time of transit center, BJD_UTC - 2,450,000

^bPlanet dayside equilibrium temperature, assuming zero albedo and uniform heat redistribution

^cGillon et al. (2009); Dragomir et al. (2011); Husnoo et al. (2012)

^dFaedi et al. (2011)

^eHartman et al. (2011)

Table 6.2. *Spitzer* Observation Details

Target	Band (μm)	UT Start Date	AOR	Duration (hrs)	n_{img} ^a	t_{int} (s) ^b	Start - End ^c	Predicted T_s ^c
WASP-6b	3.6	2009-12-30	36789248	7.6	2096	12.0	5196.19 - 5196.51	5196.3713 ± 0.0006
	4.5	2010-01-23	36788992	7.6	2096	12.0	5219.71 - 5220.03	5219.8983 ± 0.0006
WASP-39b	3.6	2012-04-04	42804992	7.0	12480	2.0	6022.04 - 6022.34	6022.2247 ± 0.0015
	4.5	2012-04-08	42804736	7.0	12480	2.0	6026.10 - 6026.39	6026.2799 ± 0.0015
HAT-P-19b	3.6	2012-03-12	42624512	7.9	14144	2.0	5999.31 - 5999.65	5999.4988 ± 0.0014
	4.5	2011-09-10	42624000	7.9	2166	12.0	5814.91 - 5815.24	5815.0950 ± 0.0011

^aTotal number of images.

^bImage integration time.

^cBJD_UTC - 2,450,000

This work focuses on analyses of the planets WASP-6b, WASP-39b, and HAT-P-19b. These represent preliminary results from a wider program utilizing *Spitzer* observations of secondary eclipses for 15 additional exoplanets, designed to search for correlations between planet mass and atmospheric metallicity. We selected planets with predicted temperatures ranging between 650-1100 K, which are predicted to have strong methane absorption features in their emission spectra if they have hydrogen-rich atmospheres whose chemistry is in local thermal equilibrium. These first three targets therefore provide a useful baseline for comparison to other current and future analyses of cooler planet atmospheres. Details of the system properties for these targets measured from radial velocity and transit observations are collected in Table 6.1. In Section 6.3, we describe the *Spitzer* data acquisition and reduction, while Sections 6.4 and 6.5 discuss the implications of these results for the properties of these planets' atmospheres.

Table 6.3. Best Fit Eclipse Model Results

Target	Band (μm)	F_p/F_* (%)	T_s^a	$e \cos \omega$
WASP-6b	3.6	0.1114 ± 0.0380	5196.3588 ± 0.0091	-0.006 ± 0.009
	4.5	0.0965 ± 0.0351	5219.8858 ± 0.0091	
WASP-39b	3.6	0.0603 ± 0.0173	6022.2418 ± 0.0039	0.007 ± 0.004
	4.5	0.0484 ± 0.0211	6026.2970 ± 0.0039	
HAT-P-19b	3.6	0.0840 ± 0.0221	5999.5066 ± 0.0048	-0.006 ± 0.005
	4.5	0.0452 ± 0.0377	5815.1028 ± 0.0048	

^aBJD_UTC - 2,450,000

6.3 Observations and Data Analysis

6.3.1 Photometry and Intrapixel Sensitivity

These observations were obtained using the Infra-Red Array Camera (IRAC) in the 3.6 and 4.5 μm channels. We padded the light curves with additional time before the predicted center of eclipse in case it was necessary to trim the initial data, as previous observations with *Spitzer* have found that the initial ~ 30 minutes of a new pointing is more sensitive to pointing drift and possible telescope focus changes. This results in a slightly off-center observation window for each of our targets with regards to their predicted eclipse times. Additional observation details can be found in Table 6.2.

In all data sets, we extract flux information from the BCD files provided by the *Spitzer* pipeline. After background subtraction, we calculate the flux using techniques described in several previous studies (Knutson et al., 2012; Lewis et al., 2013; Todorov et al., 2013; Kammer et al., 2014). First, we find the center of the stellar point spread function using a flux-weighted centroiding routine, then we perform aperture photometry, testing both fixed and time variable aperture sizes. The time variable apertures were scaled based on the noise pixel parameter (Mighell, 2005), which is proportional to the square of the full width half max of the stellar point spread function, and described by Equation 6.1 below:

$$\beta = \frac{(\sum_n I_n)^2}{\sum_n I_n^2} \quad (6.1)$$

where I_n is the measured intensity of the n^{th} pixel. We then iteratively re-scale the noise pixel aperture radii as $r = a\sqrt{\beta} + C$, where a is a scaling factor between 0.0 and 1.5 pixel widths, and C is a constant between 1.0 and 3.0 pixel widths.

We account for variations in intrapixel sensitivity using two different methods. First, we adopt a nearest neighbor weighting algorithm, such that the flux at each time step is normalized by a weighted sum of its 50 nearest neighbors in X and Y space on the pixel array, as described in Knutson et al. (2012), Lewis et al. (2013), and Kammer et al. (2014); this method has been very

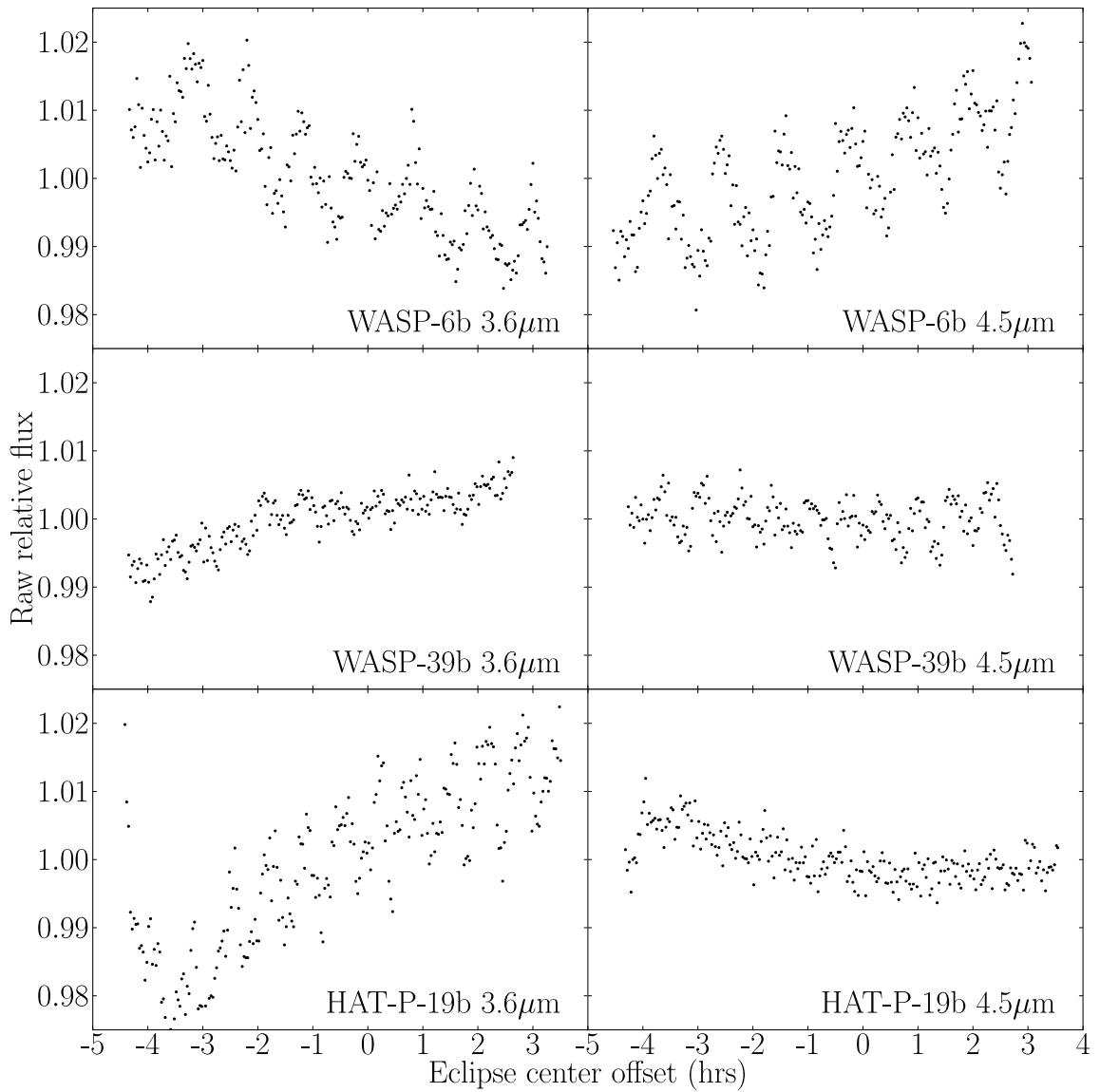


Figure 6.1 Raw *Spitzer* 3.6 and 4.5 μm light curves. The raw relative flux is shown binned at 2 minute intervals. Intrapixel sensitivity variations cause distinct sawtooth patterns as a result of the X and Y center position of the stellar point spread function oscillating over time. Observation time is shown relative to expected time of eclipse center in hours.

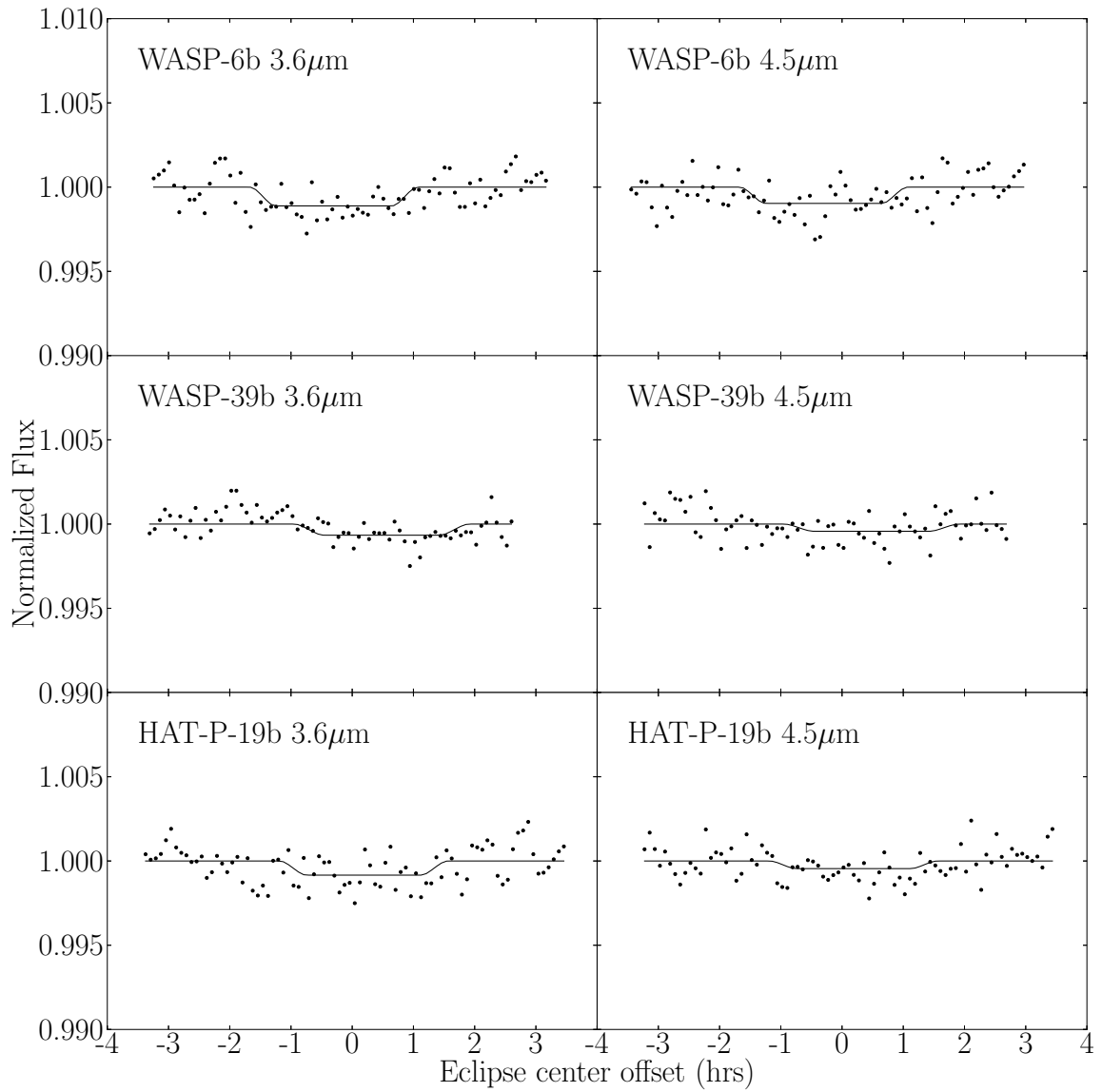


Figure 6.2 Normalized *Spitzer* 3.6 and 4.5 μm light curves. The normalized flux is shown binned at 5 minute intervals, and best fit eclipse model light curves are shown for comparison (solid lines). Observation time is shown relative to expected time of eclipse center in hours.

successful compared to a simple polynomial decorrelation for long (>10 hour) observations and for bright stars. Second, we also utilize a pixel-level decorrelation (PLD) method. Details of this PLD technique are described in Deming et al. (2014), but the basic methodology is as follows. First, we obtain the raw flux values of the pixel enclosing the stellar center as well as of the surrounding 8 pixels on the array, and then normalize by the sum of all pixels in this 3 by 3 box. This results in a set of values with the astrophysical signal of the star removed (as it proportionally affects each of the pixels equally in the time domain), and the remaining time-variability of measured flux is only due to movement of the stellar center on the array and corresponding pixel sensitivity effects. Equation 6.2 shows the resulting forward model, including the eclipse (discussed in further detail in §6.3.2).

$$F_{model}(t) = \frac{\sum_i w_i F_i(t)}{\sum_i F_i(t)} \cdot \mu(t) \quad (6.2)$$

Both methods are combined along with both fixed and time variable aperture radius models to find the lowest resulting scatter in the residuals of the fitted light curve. For these datasets, the PLD method combined with a fixed aperture radius obtains the best fit. Figure 6.1 shows the raw photometry and Figure 6.2 shows the corresponding normalized photometry after processing with this method.

6.3.2 Eclipse Models and Uncertainty Estimation

The forward model for an eclipse (Mandel & Agol, 2002) takes as input the two free parameters of time of eclipse center and planet-star flux ratio, as well as the fixed parameters of orbital period, inclination, and semi-major axis as determined from transit measurements.

Best fit model uncertainties are estimated based on a Markov chain Monte Carlo (MCMC) exploration of all forward model parameters with an effective chain length of 100,000. Model 1- σ uncertainties are represented as the 68.2% confidence interval for the posterior distributions of time of eclipse center and eclipse depth.

6.4 Discussion

The *Spitzer* observations also constrain the eccentricity of the planetary orbits. The best fit models suggest that a small, near-zero eccentricity is preferred for all targets, including WASP-39b, which was previously fixed to zero in fits to RV measurements. The eclipse-derived eccentricities, in terms of $e \cos \omega$, are listed in Table 6.3. In all cases the orbits are consistent with circular.

We next compare the measured *Spitzer* secondary eclipse depths for each planet to the predictions of standard atmosphere models. We consider two classes of models, based on Burrows et al. (2008)

and Fortney et al. (2008). Both models assume that the chemistry of these atmospheres is in local thermal equilibrium, and parameterize the unknown recirculation of energy to the night side.

We use the Fortney et al. models to explore a range of atmospheric metallicities from 1-1000x solar. Figure 6.3 shows an example of how a change in atmospheric metallicity affects the observed *Spitzer* 3.6 and 4.5 micron fluxes for WASP-6b. Figure 6.4 shows the comparison of observed data to the 1x and 1000x solar metallicity models for all three planets, with either efficient or inefficient recirculation of atmospheric heating. The relative efficiency of recirculation is implemented by varying the amount of flux incident at the top of the 1-D atmospheric column. For the inefficient case, the incident flux is set equal to the dayside average value, while for the efficient case the incident flux is calculated as the average over the entire surface. The measured eclipse depths for all three planets appear to be consistent with the solar metallicity models, although the relatively high level of 3.6 μm flux from HAT-P-19b is best matched by the 1000x solar model. All three planets also favor atmospheric models with relatively efficient heat recirculation from dayside to nightside, although the difference is only statistically significant for WASP-39b.

We next consider the suite of models from Burrows et al., which allow us to artificially create atmospheric temperature inversions and examine their effect on the shape of the observed spectrum. Figure 6.5 shows the comparison of observed data to these models, which also consider a range of redistribution efficiencies. Temperature inversions are created by adding a generalized gray absorber in the stratosphere with an absorption coefficient κ of $0.03 \text{ cm}^2 \text{ g}^{-1}$. A dimensionless parameter P_n describes the efficiency of energy redistribution, with $P_n = 0.0$ indicating recirculation on the dayside only, and $P_n = 0.5$ indicating energy evenly recirculated to the nightside as well. In these models the redistribution is implemented via a heat sink located in the lower regions of the atmosphere. In all cases, atmospheric models with temperature inversions did not appear to be significantly preferred over those without, and models with efficient recirculation of heating appear more likely than inefficient models.

6.5 Conclusions

Unlike GJ 436b, the three planets we analyzed mostly conform to the expectations of equilibrium chemistry models of 1x solar metallicity. Atmospheres without a temperature inversion are preferred over those with an inversion for these planets, but it is apparent that there can be significant degeneracy between the factors of atmospheric metallicity, recirculation efficiency, and the existence of temperature inversions. Further observations of these planets and others in a similar temperature and mass range will provide a better understanding of the underlying trends in atmospheric emission ratios, and in the future, improved spectroscopic coverage in general will yield more leverage in uniquely identifying species abundances derived from secondary eclipse observations.

6.6 Acknowledgements

J.-M.D. acknowledges funding from NASA through the Sagan Exoplanet Fellowship program administered by the NASA Exoplanet Science Institute (NExSci). This work is based on observations made with the *Spitzer Space Telescope*, which is operated by the Jet Propulsion Laboratory, California Institute of Technology, under contract with NASA.

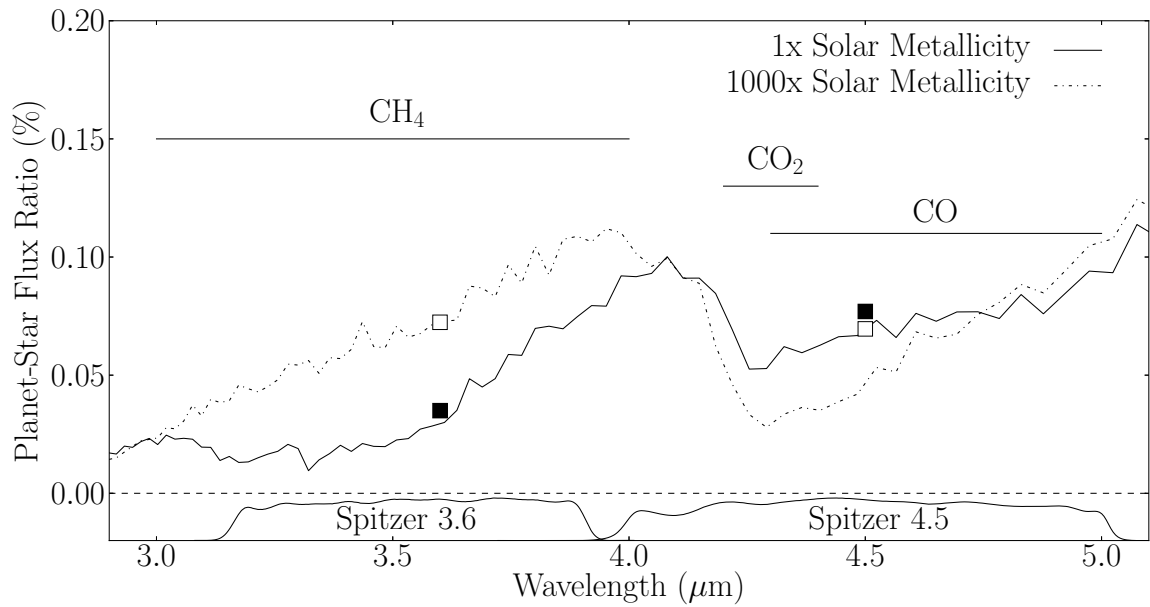


Figure 6.3 Atmospheric metallicity affects the CH_4 to CO ratio and the planet-star flux ratio as seen by *Spitzer*. The general regions of absorption by CH_4 , CO_2 , and CO are indicated, while the transmission function of the *Spitzer* 3.6 and 4.5 micron bands are shown at the bottom of the plot in arbitrary units. Solar metallicity (solid line) and high metallicity (dash-dotted line) models are also plotted, with the effective flux ratios as seen by *Spitzer* indicated by the black and white squares, respectively. Models from Fortney et al. (2008).

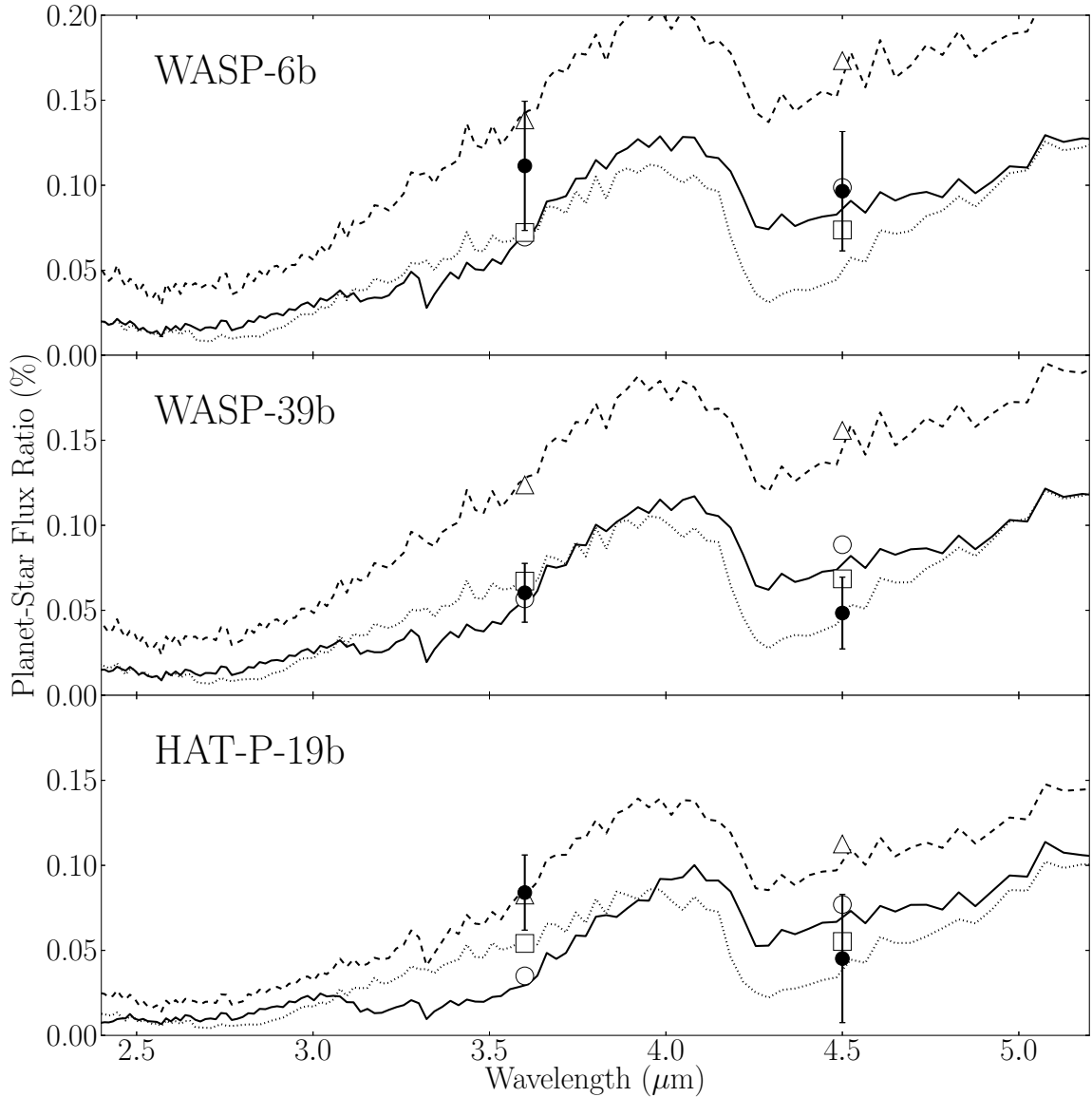


Figure 6.4 Planet-star flux models of different atmospheric metallicities compared to the *Spitzer* 3.6 and 4.5 micron secondary eclipse observations, with their associated 1- σ uncertainties. Shown are models for 1x solar (solid line, white circles), and 1000x solar (dotted line, squares) atmospheric metallicity with efficient recirculation of atmospheric heating. Also shown are 1x solar metallicity models with inefficient heat recirculation (dashed line, triangles). Models from Fortney et al. (2008).

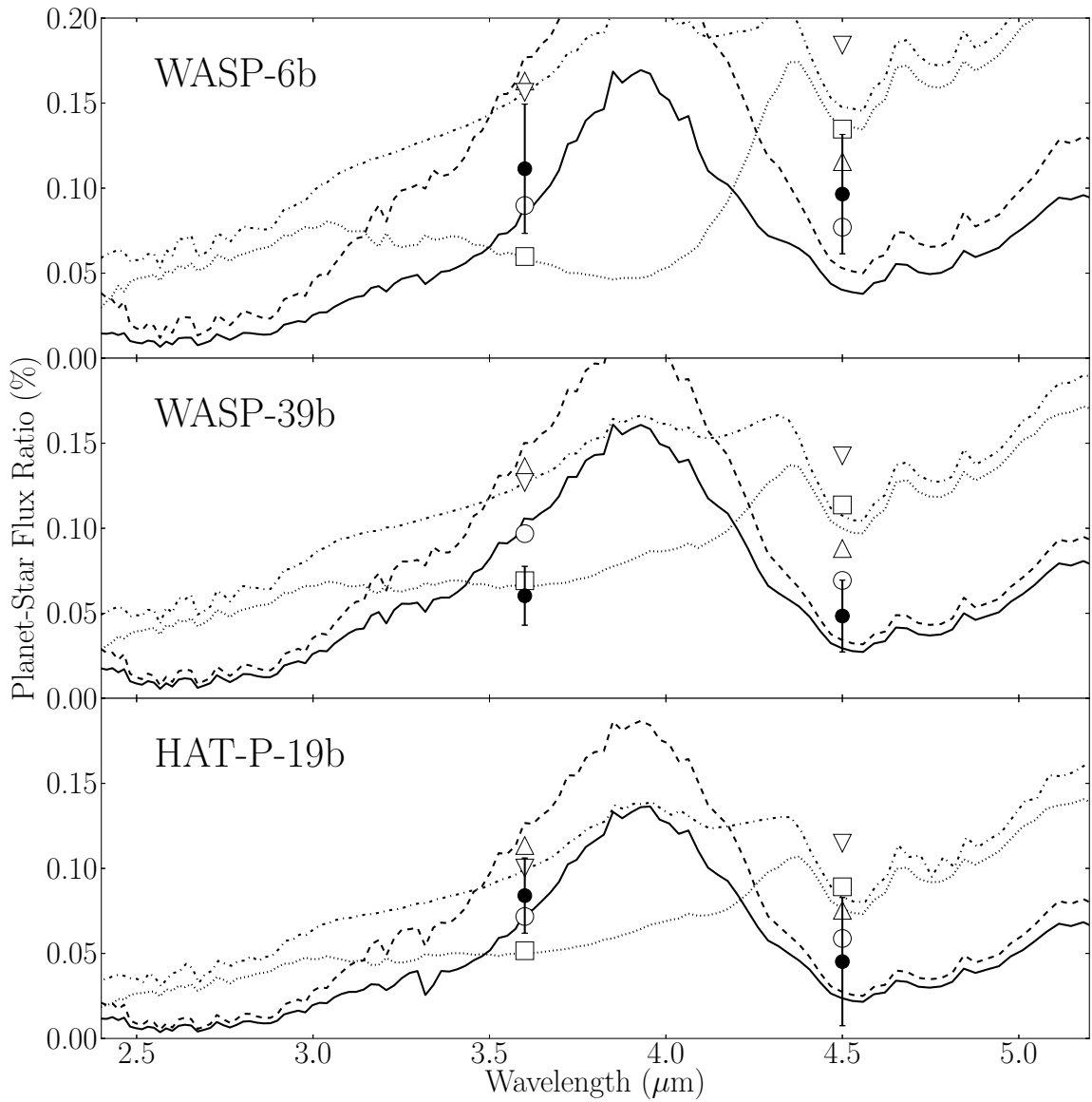


Figure 6.5 Planet-star flux models showing the effect of a possible temperature inversion in the atmosphere. Shown are models for no inversion, efficient heat recirculation (solid line, white circles); no inversion, inefficient recirculation (dashed line, upright triangles); with inversion, efficient recirculation (dotted line, squares); and with inversion, inefficient recirculation (dash-dotted line, inverted triangles). Models from Burrows et al. (2008).

Bibliography

- Burrows, A., et al. 2008, *The Astrophysical Journal*, 678, 1436
- Cubillos, P., et al. 2013, *The Astrophysical Journal*, 768, 42
- Deming, D., et al. 2014, *The Astrophysical Journal*, in prep.
- Dragomir, D., et al. 2011, *The Astronomical Journal*, 142, 115
- Faedi, F., et al. 2011, *Astronomy and Astrophysics*, 531, A40
- Fortney, J. J., et al. 2008, *The Astrophysical Journal*, 678, 1419
- Gillon, M., et al. 2009, *Astronomy and Astrophysics*, 501, 785
- Hartman, J. D., et al. 2011, *The Astrophysical Journal*, 726, 52
- Helled, R. & Bodenheimer, P. 2014, *The Astrophysical Journal*, 789, 69
- Husnoo, N., et al. 2012, *Monthly Notices of the Royal Astronomical Society*, 422, 3151
- Kammer, J. A., et al. 2014, *The Astrophysical Journal*, 781, 103
- Kirkpatrick, J. D. 2005, *Annual Review of Astronomy and Astrophysics*, 43, 195
- Knutson, H. A., et al. 2012, *The Astrophysical Journal*, 754, 22
- Lewis, N. K., et al. 2013, *The Astrophysical Journal*, 766, 95
- Line, M. R., et al. 2011, *The Astrophysical Journal*, 738, 32
- Mandel, K., & Agol, E. 2002, *The Astrophysical Journal Letters*, 580, L171
- Madhusudhan, N., et al. 2014, *Protostars and Planets VI*, University of Arizona Press
- Mighell, K. J. 2005, *Monthly Notices of the Royal Astronomical Society*, 361, 861
- Moses, J. I., et al. 2013, *The Astrophysical Journal*, 777, 34
- Stevenson, K. B., et al. 2010, *Nature*, 464, 1161
- Todorov, K. O., et al. 2013, *The Astrophysical Journal*, 770, 102